This project has received funding from the European Union's Horizon Europe research and innovation programme under grant agreement No 101056732

NEXTAIR

multi-disciplinary digital-enablers for NEXT-generation AIRcraft design and operations

D1.2 - ASSESSMENT OF TRANSITION MODELS & THEIR ADJOINTS

Document authors	Kyriakos Giannakoglou (NTUA) Marina Kontou (NTUA) Cosimo Tarsia Morisco (INRIA) Gilbert Rogé (DAV)
Document contributors	Xenofon Trompoukis (NTUA)

Abstract

In WP1, among other, (laminar-to-turbulent flow) transition models for solvers of the RANS equations will be developed and their adjoint codes will be programmed and used in shape optimization problems. This work will be done by three NEXTAIR partners, namely NTUA, DAV and INRIA using different codes and different adjoint methods. NTUA used the in-house GPU-accelerated PUMA code, based on vertex-centered finite volumes. DAV used code AETHER that uses the finite element method on unstructured grids. The transition models used are four variants of the $\gamma - \tilde{Re}_{\theta t}$ standard model, coupled occasionally with the Spalart-Allmaras and $k-\omega$ SST turbulence models or stability analysis with the eN approach (only DAV). Very good comparisons among codes and measurements in the NLF(1)-0416 isolated airfoil case are presented. Regarding optimization, NTUA is using continuous adjoint, whereas DAV and INRIA discrete adjoint. The developed adjoint codes have been used first to verify the accuracy of the computed sensitivity derivatives which is adequately demonstrated in this report. It is interesting to note the very good agreement between not only absolutely different flow solvers but, also, continuous and discrete adjoint. Once the agreement of the computed gradients of objective functions with respect to the design variables has been verified, next step is the use of these tools to run demo optimization cases.

Keywords

CFD, Transitional Flows, Modeling of Transition, Optimization, Continuous and Discrete Adjoint, Aerodynamics

Funded by the European Union. Views and opinions expressed are however those of the author(s) only and do not necessarily reflect those of the European Union. Neither the European Union nor the granting authority can be held responsible for them.

Information Table

PROJECT INFORMATION	
PROJECT ID	101056732
PROJECT FULL TITLE	NEXTAIR - multi-disciplinary digital - enablers for NEXT-generation AIRcraft design and operations
PROJECT ACRONYM	NEXTAIR
START DATE OF THE PROJECT	01/09/2022
DURATION	36 months
CALL IDENTIFIER	HORIZON-CL5-2021-D5-01
PROJECT WEBSITE	https://www.nextair-project.eu/

DELIVERABLE INFORMATION	
DELIVERABLE No AND TITLE	D1.2 - Assessment of transition models & their adjoints
TYPE OF DELIVERABLE	R
DISSEMINATION LEVEL	PU
BENEFICIARY NUMBER AND NAME	7-NTUA
AUTHORS	see first page
CONTRIBUTORS	see first page
WORK PACKAGE No	1
WORK PACKAGE LEADER	NTUA
COORDINATOR VALIDATION DATE	10/11/2023

1 Contributions by PUMA

1.1 Transition Modeling in PUMA

1.1.1 The URANS Equations for Compressible Flows

In the URANS equations, the mean flow equations for compressible fluid flows are solved in the form

$$R_n^{\text{MF}} = \frac{\partial U_n}{\partial t} + \frac{\partial f_{nk}^{\text{inv}}}{\partial x_k} - \frac{\partial f_{nk}^{\text{vis}}}{\partial x_k} = 0 \tag{1.1.1}$$

Eq. 1.1.1 is solved for the conservative flow variables $U_n = [\rho \;\; \rho v_1 \;\; \rho v_2 \;\; \rho v_3 \;\; \rho E]^T$, where ρ stands for the fluid density, $v_m\,(m=1,2,3)$ being the velocity components and E the total energy per unit mass. In Eq. 1.1.1 $f_{nk}^{\text{inv}} = [\rho v_k \;\; \rho v_k v_1 + p\delta_{1k} \;\; \rho v_k v_2 + p\delta_{2k} \;\; \rho v_k v_3 + p\delta_{3k} \;\; \rho v_k h_t]$ are the inviscid and $f_{nk}^{\text{vis}} = [0 \;\; \tau_{1k} \;\; \tau_{2k} \;\; \tau_{3k} \;\; v_\ell \tau_{\ell k} + q_k]$ the viscous fluxes. p, h_t stand for the fluid's pressure and total enthalpy and δ_{km} is the Kronecker symbol. $\tau_{km} = (\mu + \mu_t)\left(\frac{\partial v_k}{\partial x_m} + \frac{\partial v_m}{\partial x_k} - \frac{2}{3}\delta_{km}\frac{\partial v_\ell}{\partial x_\ell}\right)$ is the stress tensor, $q_k = C_p\left(\frac{\mu}{\text{Pr}} + \frac{\mu_t}{\text{Pr}_t}\right)\frac{\partial T}{\partial x_k}$ is the heat flux, where μ, μ_t are the molecular and turbulent viscosity, respectively. Pr, Pr_t stand for the constant Prandtl and turbulent Prandtl number and C_p is the fluid's specific heat capacity at constant pressure. For a perfect gas, temperature T is related to p and ρ through the equation of state $p = \rho R_g T$, with R_g being the specific gas constant.

Turbulent viscosity μ_t is computed either by employing the one-equation Spalart-Allmaras (34) or the two-equation Menter's $k-\omega\; SST$ (26) turbulence models.

For the Spalart-Allmaras model, (34), an additional PDE is solved for $\tilde{\nu}$, namely

$$\begin{aligned} R^{\tilde{\nu}} = & \frac{\partial(\rho\tilde{\nu})}{\partial t} + \frac{\partial(\rho\tilde{\nu}v_k)}{\partial x_k} - \frac{\rho}{\sigma}\left\{\frac{\partial}{\partial x_k}\left[(\nu+\tilde{\nu})\frac{\partial\tilde{\nu}}{\partial x_k}\right] + c_{b_2}\frac{\partial\tilde{\nu}}{\partial x_k}\frac{\partial\tilde{\nu}}{\partial x_k}\right\} \\ & - \rho c_{b_1}(1-f_{t_2})\tilde{S}\tilde{\nu} + \rho\left(c_{w_1}f_w - \frac{c_{b_1}}{\kappa^2}f_{t_2}\right)\left(\frac{\tilde{\nu}}{\Delta}\right)^2 = 0 \end{aligned} \tag{1.1.2}$$

where Δ is the distance of each point within the flow domain from the closest solid wall, and μ_t is given by $\mu_t = \rho\tilde{\nu}f_{v_1}$. Eq. 1.1.2 is supplemented by the following relations (34): $\chi = \frac{\tilde{\nu}}{\nu}$, $f_{v_1} = \frac{\chi^3}{\chi^3 + c_{v_1}^3}$, $f_{v_2} = 1 - \frac{\chi}{1+\chi f_{v_1}}$, $\zeta = \sqrt{\varepsilon_{k\ell m}\varepsilon_{kqr}\frac{\partial v_m}{\partial x_\ell}\frac{\partial v_r}{\partial x_q}}$, $\tilde{S} = \zeta + \frac{\tilde{\nu}f_{v_2}}{\kappa^2\Delta^2}$, $f_w = g\left(\frac{1+c_{w_3}^6}{g^6 + c_{w_3}^6}\right)^{\frac{1}{6}}$, $g = r + c_{w_2}(r^6 - r)$, $r = \min\left(10, \frac{\tilde{\nu}}{\tilde{S}\kappa^2\Delta^2}\right)$, $\tilde{\mu} = \rho\tilde{\nu}$, $f_{t_2} = c_{t_3}e^{-c_{t_4}\chi^2}$. Also, $c_{v_1} = 7.1, c_{b_1} = 0.1355, c_{b_2} = 0.622, c_{w_1} = \frac{c_{b_1}}{\kappa^2} + \frac{1+c_{b_2}}{\sigma}, c_{w_2} = 0.3, c_{w_3} = 2.0, \sigma = \frac{2}{3}, \kappa = 0.41, c_{t_3} = 1.2, c_{t_4} = 0.5$

On the other hand, the Menter's $k-\omega\; SST$ model, (26), solves two PDEs for the turbulent kinetic energy k and the specific dissipation rate ω,

$$\begin{aligned} R^k &= \frac{\partial(\rho k)}{\partial t} + \frac{\partial(\rho k v_k)}{\partial x_k} - \frac{\partial}{\partial x_k}\left[(\mu + \sigma_k\mu_t)\frac{\partial k}{\partial x_k}\right] - \tilde{P}_\kappa + \beta^*\rho k\omega = 0 \\ R^\omega &= \frac{\partial(\rho\omega)}{\partial t} + \frac{\partial(\rho\omega v_k)}{\partial x_k} - \frac{\partial}{\partial x_k}\left[(\mu + \sigma_\omega\mu_t)\frac{\partial\omega}{\partial x_k}\right] \\ & \quad - \gamma\frac{P_\kappa}{\nu_t} + \beta\rho\omega^2 - 2(1-F_1)\frac{\rho\sigma_{\omega_2}}{\omega}\frac{\partial k}{\partial x_k}\frac{\partial\omega}{\partial x_k} = 0 \end{aligned} \tag{1.1.3}$$

This model combines the standard $k-\omega$ and $k-\varepsilon$ models, so any constant ϕ is blended using function F_1 (its definition is given below) which is equal to 1.0 close to rigid walls and 0.0 far from them as follows: $\phi = F_1\phi_1 + (1-F_1)\phi_2$. Upon solution of Eq. 1.1.3 , μ_t is computed as $\mu_t = \frac{\rho a_1 k}{\max(a_1\omega, SF_2)}$. The model is supplemented by the following relations and constants: $F_1 = tanh\left(min\left(arg_{F1}^4, 10\right)\right)$, $F_2 =$

$tanh\left(min\left(arg_{F2}^2, 100\right)\right), arg_{F1}=min\left(max\left(\frac{\sqrt{k}}{\beta^*\omega y}, \frac{500\nu}{\omega y^2}\right), \frac{4\rho k\sigma_{\omega 2}}{CD_{k\omega}y^2}\right), arg_{F2}=max\left(\frac{2\sqrt{k}}{\beta^*\omega y}, \frac{500\nu}{\omega y^2}\right)$, $CD_{k\omega}=max\left(\frac{2\rho\sigma_{\omega 2}}{\omega}\frac{\partial k}{\partial x_k}\frac{\partial \omega}{\partial x_k}, e^{-10}\right)$, $\tilde{P}_\kappa=\min\left(P_\kappa, 10\beta^*\rho k\omega\right)$, $P_\kappa=\mu_t S^2-\frac{2}{3}\rho k\delta_{km}\frac{\partial v_m}{\partial x_k}$, $S=\sqrt{2S_{km}S_{km}}$, $S_{km}=\frac{1}{2}\left(\frac{\partial v_m}{\partial x_k}+\frac{\partial v_k}{\partial x_m}\right)$, $\sigma_{k1}=0.85034,\ \sigma_{k2}=0.5,\ \beta_1=0.075,\ \gamma_1=5/9,\ \alpha_1=0.31,$ $\sigma_{k2}=1.0,\ \sigma_{\omega 2}=0.85616,\ \beta_2=0.0828,\ \gamma_2=0.44,\ \beta^*=0.09.$

1.1.2 The $\gamma-\tilde{R}e_{\theta t}$ Transition Model

The above two turbulence models are coupled with the two equation $\gamma-\tilde{R}e_{\theta t}$ transition model, (19). Two additional PDEs are solved for the transition intermittency γ and the transition momentum-thickness Reynolds number $\tilde{R}e_{\theta t}$. These are

$$\begin{aligned} R^{\gamma} &= \frac{\partial\left(\rho\gamma\right)}{\partial t}+\frac{\partial\left(\rho v_k\gamma\right)}{\partial x_k}-\frac{\partial}{\partial x_k}\left[\left(\mu+\frac{\mu_t}{\sigma_f}\right)\frac{\partial\gamma}{\partial x_k}\right]-P_\gamma+E_\gamma=0 \\ R^{\tilde{R}e_{\theta t}} &= \frac{\partial\left(\rho\tilde{R}e_{\theta t}\right)}{\partial t}+\frac{\partial\left(\rho v_k\tilde{R}e_{\theta t}\right)}{\partial x_k}-\frac{\partial}{\partial x_k}\left[\sigma_{\theta,t}\left(\mu+\mu_t\right)\frac{\partial\tilde{R}e_{\theta t}}{\partial x_k}\right] \\ &\quad -P_{\theta,t}-D_{SCF}=0 \end{aligned} \tag{1.1.4}$$

The original $\gamma-\tilde{R}e_{\theta t}$ transition model by Langtry and Menter in (19) and extended to accommodate stationary crossflow effects in (18) was developed for the $k-\omega\ SST$ turbulence model. In (14, 13, 28) source terms were modified for this transition model to collaborate with the Spalart-Allmaras model. Expressions of P_γ, E_γ, $P_{\theta,t}$ and D_{SCF}, as well as their interaction with the turbulence models follow. Four transition model variants are used, Sec. 1.1.2 presents the SST-2003-LM2015 transition model coupled with the $k-\omega\ SST$ model and Secs. 1.1.2, 1.1.2 and 1.1.2 the SA-noft2-Gamma-Retheta, SA-LM2015 and SA-sLM2015 transition models coupled with the Spalart-Allmaras model.

The SST-2003-LM2015 Transition Model

In the original $\gamma-\tilde{R}e_{\theta t}$ transition model, (19, 18), which is coupled with the $k-\omega\ SST$ model, the source terms for the γ equation are defined as follows:

$$P_\gamma=\rho c_{\alpha_1}S\sqrt{\gamma F_{onset}}\left(1-c_{\epsilon_1}\gamma\right)F_{length},\quad E_\gamma=\rho c_{\alpha_2}\zeta\gamma F_{turb}\left(c_{\epsilon_2}\gamma-1\right)$$

where S and ζ are the strain rate and the vorticity magnitude, respectively. Also,

$$\begin{aligned} &F_{onset}=\max\left(F_{onset2}-F_{onset3}, 0\right),\quad F_{onset2}=\min\left[\max\left(F_{onset1}, F_{onset1}^4\right), 2\right] \\ &F_{onset3}=\max\left[\left(1-\left(\frac{R_T}{2.5}\right)^3\right), 0\right],\quad F_{onset1}=\frac{Re_\nu}{2.193Re_{\theta c}},\quad Re_\nu=\frac{\rho S\Delta^2}{\mu},\quad R_T=\frac{\rho k}{\mu\omega} \end{aligned}$$

F_{length} and $Re_{\theta c}$ are functions of $\tilde{R}e_{\theta t}$ based on the following empirical correlations:

$$F_{length}{=}F_{length1}(1-F_{sublayer})+40F_{sublayer},\quad F_{sublayer}=e^{-\left(\frac{R_\omega}{0.4}\right)^2},\quad R_\omega=\frac{\rho\Delta^2\omega}{500\mu}$$

$$F_{length1}{=}\begin{cases}398.189e^{-1}-119.270e^{-4}\tilde{R}e_{\theta t}-132.567e^{-6}\tilde{R}e_{\theta t}^2 & \text{, if } \tilde{R}e_{\theta t}<400\\ 263.404-123.939e^{-2}\tilde{R}e_{\theta t}+194.548e^{-5}\tilde{R}e_{\theta t}^2 & \\ \quad -101695e^{-8}\tilde{R}e_{\theta t}^3 & \text{, if } 400\leq\tilde{R}e_{\theta t}<596\\ 0.5-\left(\tilde{R}e_{\theta t}-596\right)3e^{-4} & \text{, if } 596\leq\tilde{R}e_{\theta t}<1200\\ 0.3188 & \text{, if } 1200\geq\tilde{R}e_{\theta t}\end{cases}$$

$$Re_{\theta c}{=}\begin{cases}\tilde{R}e_{\theta t}-396.035e^{-2}+120.656e^{-4}\tilde{R}e_{\theta t}-868.23e^{-6}\tilde{R}e_{\theta t}^2 & \\ +696.506e^{-9}\tilde{R}e_{\theta t}^3-174.105e^{-12}\tilde{R}e_{\theta t}^4 & \text{, if } \tilde{R}e_{\theta t}\leq 1870\\ \tilde{R}e_{\theta t}-593.11-\left(\tilde{R}e_{\theta t}-1870\right)0.482 & \text{, if } \tilde{R}e_{\theta t}>1870\end{cases}$$

In the destruction term E_γ, F_{turb} is used and this is defined as

$$F_{turb}{=}\exp\left[-\left(\frac{R_T}{4}\right)^4\right]$$

The source terms $P_{\theta,t}$ and D_{SCF} in the $\tilde{R}e_{\theta t}$ equation are expressed as

$$P_{\theta,t}=\rho\frac{c_{\theta,t}}{\mathcal{T}}\left(Re_{\theta,t}^{eq}-\tilde{R}e_{\theta t}\right)(1-F_{\theta t}),\quad D_{SCF}=c_{\theta,t}\frac{\rho}{\mathcal{T}}c_{crossflow}\min\left(Re_{SCF}-\tilde{R}e_{\theta t},0\right)F_{\theta t2}$$

The blending function $F_{\theta t}$ and the timescale T are defined as

$$F_{\theta t}{=}\min\left[\max\left[F_{wake}\exp\left[-\left(\frac{\Delta}{\delta}\right)^4\right],1-\left(\frac{\gamma-1/c_{\epsilon_2}}{1-1/c_{\epsilon_2}}\right)^2\right],1\right]$$

$$F_{wake}{=}exp\left[-\left(\frac{Re_\omega}{10^5}\right)^2\right],\quad Re_\omega{=}\frac{\rho\omega\Delta^2}{\mu}$$

$$\mathcal{T}{=}\frac{500\mu}{\rho\left|\mathbf{U}\right|^2},\quad \delta{=}\frac{375\zeta\mu\tilde{R}e_{\theta t}\Delta}{\rho\left|\mathbf{U}\right|^2},\quad \left|\mathbf{U}\right|{=}\sqrt{v_\ell v_\ell},\ (\ell{=}1,\ldots,3)$$

$Re_{\theta,t}^{eq}$ is a function of the turbulence intensity Tu and the pressure gradient parameter λ_θ:

$$Tu{=}100\frac{\sqrt{2k/3}}{\left|\mathbf{U}\right|},\quad \lambda_\theta{=}\frac{\rho\theta^2}{\mu}\frac{d\left|\mathbf{U}\right|}{ds},\quad \frac{d\left|\mathbf{U}\right|}{ds}{=}\frac{v_m v_n}{\left|\mathbf{U}\right|^2}\frac{\partial v_m}{\partial x_n} \tag{1.1.5}$$

$$Re_{\theta,t}^{eq}{=}\begin{cases}\left(1173.51-589.428Tu+0.2196/Tu^2\right)F\left(\lambda_\theta\right) & \text{, if } Tu\leq 1.3\\ 331.5\left(Tu-0.5668\right)^{-0.671}F\left(\lambda_\theta\right) & \text{, if } Tu>1.3\end{cases} \tag{1.1.6}$$

where

$$F\left(\lambda_\theta\right){=}\begin{cases}1+\left[12.986\lambda_\theta+123.66\lambda_\theta^2+405.689\lambda_\theta^3\right]\exp\left[-\left(\frac{Tu}{1.5}\right)^{1.5}\right] & \text{, if } \lambda_\theta\leq 0\\ 1+0.275\left[1-\exp\left(-35\lambda_\theta\right)\right]\exp\left(-\frac{Tu}{0.5}\right) & \text{, if } \lambda_\theta>0\end{cases} \tag{1.1.7}$$

$Re_{\theta,t}^{eq}$ is an implicit function of θ through the presence of λ_θ since $Re_{\theta,t}^{eq}=\frac{\rho|\mathbf{U}|\theta}{\mu}$. Equations 1.1.5- 1.1.7 can be solved by iterating on the value of θ. For numerical robustness, λ_θ, Tu and $Re_{\theta,t}^{eq}$ should be limited as follows:

$$-0.1\leq\lambda_\theta\leq 0.1,\quad Tu\geq 0.027,\quad Re_{\theta,t}^{eq}\geq 20$$

The stationary crossflow instabilities are present mainly due to the surface roughness (h_{rms}), (18). Regarding the source term related to the stationary crossflow effects D_{SCF}, $F_{\theta t2}$ stands for a crossflow sink term, active only inside the laminar boundary layer. Timescale $\mathcal{T}$ is limited for robustness reasons based on the local grid length L,

$$Re_{SCF} = \frac{\rho\theta_t |\mathbf{U}|}{0.82\mu} = -35.088 \ln\left(\frac{h_{rms}}{\theta_t}\right) + 319.51 + f\left(\mathcal{D}H_{CF+}\right) - f\left(\mathcal{D}H_{CF-}\right)$$

$$f\left(\mathcal{D}H_{CF+}\right) = 6200\mathcal{D}H_{CF+} + 5000\left(\mathcal{D}H_{CF+}\right)^2, \quad f\left(\mathcal{D}H_{CF-}\right) = 75\tanh\left(\frac{\mathcal{D}H_{CF-}}{0.0125}\right)$$

$$\mathcal{D}H_{CF+} = \max\left[+\left(0.1066 - \mathcal{D}H_{CF}, 0\right)\right], \quad \mathcal{D}H_{CF-} = \max\left[-\left(0.1066 - \mathcal{D}H_{CF}, 0\right)\right]$$

$$\mathcal{D}H_{CF} = H_{CF}\left[1 + \min\left(\frac{\mu_t}{\mu}, 0.4\right)\right], \quad H_{CF} = \frac{\zeta_{streamwise}\Delta}{|\mathbf{U}|}, \quad \zeta_{streamwise} = \left|\vec{U}\cdot\vec{\zeta}\right|$$

$$F_{\theta t2} = \min\left(F_{wake}\exp\left(-\left(\Delta/\delta\right)^4\right), 1\right), \quad \mathcal{T} = \min\left(\frac{500\mu}{\rho|\mathbf{U}|^2}, \frac{\rho L^2}{(\mu + \mu_t)}\right)$$

The model constants are $c_{\alpha_1} = 2$, $c_{\alpha_2} = 0.06$, $c_{\epsilon_1} = 1$, $c_{\epsilon_2} = 50$, $c_{\theta,t} = 0.03$, $\sigma_f = 1$, $\sigma_{\theta,t} = 2$, $c_{crossflow} = 0.6$. The modification to the intermittency for this to predict transition induced by flow separation is

$$\gamma_{sep} = \min\left(2\max\left[0, \left(\frac{Re_\nu}{3.235Re_{\theta c}}\right) - 1\right]F_{reattach}, 2\right)F_{\theta t}$$

$$F_{reattach} = \exp\left[-\left(\frac{R_T}{20}\right)^4\right], \quad \gamma_{eff} = \max\left(\gamma, \gamma_{sep}\right)$$

The following modifications to the source terms of the $k-\omega\ SST$ model,

$$\tilde{P_k} = \gamma_{eff}P_K, \quad \tilde{D_k} = min\left(max\left(\gamma_{eff}, 0.1\right), 1\right)D_k$$

$$R_y = \frac{\rho\Delta\sqrt{k}}{\mu}, \quad F_3 = e^{-\left(\frac{R_y}{120}\right)^8}, \quad F_1 = max\left(F_{1orig}, F_3\right)$$

are necessary where P_k, D_k, F_{1orig} are the original production and destruction terms and the blending function for the $k-\omega\ SST$ model.

The SA-noft2-Gamma-Retheta Transition Model

(14, 13) proposed slight modifications to the original $\gamma-\tilde{R}e_{\theta t}$ transition model of Sec. 1.1.2 in order to couple it with the Spalart-Allmaras model. The new model is denoted as SA-noft2-Gamma-Retheta. These modifications refer to the F_{onset}, F_{length} and $Re_{\theta c}$ correlations and the $F_{\theta t}$ term,

$$F_{onset} = \max\left(F_{onset2} - F_{onset3}, 0\right), \quad F_{onset2} = \min\left[\max\left(F_{onset1}, F_{onset1}^4\right), 4\right]$$

$$F_{onset3} = \max\left[\left(2 - \left(\frac{R_T}{2.5}\right)^3\right), 0\right], \quad F_{onset1} = \frac{Re_\nu}{2.193Re_{\theta c}}, \quad R_T = \frac{\mu_t}{\mu}$$

$$F_{length} = \min\left(\exp\left(7.168 - 0.01173\tilde{R}e_{\theta t}\right) + 0.5, 3000\right)$$

$$Re_{\theta c} = \min\left(0.615\tilde{R}e_{\theta t} + 61.5, \tilde{R}e_{\theta t}\right)$$

$$F_{\theta t} = \min\left[\max\left[\exp\left[-\left(\frac{\Delta}{\delta}\right)^4\right], 1 - \left(\frac{\gamma - 1/c_{\epsilon_2}}{1 - 1/c_{\epsilon_2}}\right)^2\right], 1\right]$$

In the Spalart-Allmaras model, the production term of Eq. 1.1.2 is multiplied with γ_{eff}, f_{t_2} is set to zero and the following modifications to its source terms are made:

$$\tilde{P}_{\tilde{\nu}} = \gamma_{eff}\rho c_{b_1}\tilde{S}, \;\; \tilde{D}_{\tilde{\nu}} = \rho c_{w_1} f_w \left(\frac{\tilde{\nu}}{\Delta}\right)^2, \;\; \tilde{S} = [\zeta + min\,(S-\zeta)] + \frac{\tilde{\nu} f_{v_2}}{\kappa^2\Delta^2}$$

$$r = \begin{cases} 10 & \text{, if } \frac{\tilde{\nu}}{\tilde{S}\kappa^2\Delta^2} < 0 \\ min\left(10, \frac{\tilde{\nu}}{\tilde{S}\kappa^2\Delta^2}\right) & \text{, if } \frac{\tilde{\nu}}{\tilde{S}\kappa^2\Delta^2} \geq 0 \end{cases}$$

Crossflow effects are not present. The rest of terms are similar to those described in Sec. 1.1.2.

The SA-LM2015 Transition Model

In (28), the original $\gamma - \tilde{Re}_{\theta t}$ transition model proposed by Langtry and Menter (Sec. 1.1.2) was modified by Piotrowski and Zingg and coupled with the Spalart-Allmaras model. The strain rate magnitude S was replaced with vorticity ζ, in the production term of the intermittency equation, in order to enhance the stability near the laminar separation bubbles, (28). This model is denoted as SA-LM2015. The production and destruction terms for the intermittency equation read

$$P_\gamma = \rho c_{\alpha_1} F_{length} F_{onset} \zeta \sqrt{\gamma}\,(1 - c_{\epsilon_1}\gamma)\,, \;\; E_\gamma = \rho c_{\alpha_2} F_{turb} \zeta \gamma\,(c_{\epsilon_2}\gamma - 1)$$

For the γ equation, the following modifications are made compared to the SST-2003-LM2015 transition model:

$$F_{onset} = \max\left(F_{onset2} - F_{onset3}, 0\right), \;\; F_{onset2} = \min\left[\max\left(F_{onset1}, F_{onset1}^4\right), 4\right]$$

$$F_{onset3} = \max\left[\left(2 - \left(\frac{R_T}{2.5}\right)^3\right), 0\right], \;\; F_{onset1} = \frac{Re_S}{2.193 Re_{\theta c}}, \;\; Re_S = \frac{\rho\Delta^2 S}{\mu}, \;\; R_T = \frac{\mu_t}{\mu}$$

while, for the $\tilde{Re}_{\theta t}$ equation,

$$F_{\theta t} = F_{wake} \exp\left[-\left(\frac{\Delta}{\delta}\right)^4\right], \;\; F_{wake} = \exp\left[-^{Re_S}/_{1.e^6}\right]$$

In order to interact with the Spalart-Allmaras model, the production term of Eq. 1.1.2 is multiplied with γ, f_{t_2} is set to zero and the following modifications to the Spalart-Allmaras source terms are made:

$$\tilde{P}_{\tilde{\nu}} = \gamma\rho c_{b_1}\tilde{S}\tilde{\nu}, \;\; D_{\tilde{\nu}} = \rho c_{w_1} f_w \left(\frac{\tilde{\nu}}{\Delta}\right)^2$$

The rest of terms are similar to those described in Sec. 1.1.2.

The SA-sLM2015 Transition Model

The expressions of the source terms in the transition models presented in Secs. 1.1.2, 1.1.2, 1.1.2 include min. and max. operators and conditional statements. These non-smooth functions can lead to discontinuities, during the numerical solution of the primal and adjoint equations. In (28), to overcome this, smooth approximations to the min./max. operators and simplifications to the conditional statements were introduced by Piotrowski and Zingg based on the SA-LM2015 model, giving rise to the SA-sLM2015 transition model.

The smooth min. /max. operator function ϕ_p (a positive real number $p>0$ is used for the max. operator and a negative one $p<0$ for min) for two variables x_1, x_2 is described as

$$\text{for p>0:}\;\; \phi_p\left(x_1,x_2\right)=\begin{cases}\alpha & \text{, if } |\alpha-\beta| > -\frac{\log(|p|p_{switch})}{|p|}\\ \alpha+\frac{\log(1+\exp\left[p(\beta-\alpha)\right])}{p} & \text{, else}\end{cases}$$

$$\text{for p<0:}\;\; \phi_p\left(x_1,x_2\right)=\begin{cases}\beta & \text{, if } |\alpha-\beta| > -\frac{\log(|p|p_{switch})}{|p|}\\ \beta+\frac{\log(1+\exp\left[p(\alpha-\beta)\right])}{p} & \text{, else}\end{cases}$$

$$\alpha=\max\left(x_1,x_2\right),\;\; \beta=\min\left(x_1,x_2\right),\;\; p_{switch}=10^{-15}$$

Then, the production and destruction terms of the γ PDE read

$$P_\gamma=\rho c_{\alpha_1}F_{length}F_{onset}\left[\phi_{-300}\left(\zeta,\frac{M\sqrt{MRe}}{20}\right)\right]\sqrt{\gamma}\left(1-c_{\epsilon_1}\gamma\right)$$

$$E_\gamma=\rho c_{\alpha_2}F_{turb}\left[\phi_{-300}\left(\zeta,\frac{M\sqrt{MRe}}{20}\right)\right]\gamma\left(c_{\epsilon_2}\gamma-1\right)$$

F_{onset}, F_{turb}, F_{length} and $Re_{\theta c}$ are expressed as

$$F_{onset}=\frac{\tanh\left[6\left(F_{onset1}-1.35\right)\right]+1}{2},\;\; F_{onset1}=\sqrt{\left(\frac{Re_S}{2.6Re_{\theta c}}\right)^2+\left(R_T\right)^2}$$

$$F_{length}=44-\frac{44-\left(0.50-3\cdot10^{-4}\left(\tilde{R}e_{\theta t}-596\right)\right)}{\left(1+F_{length1}\right)^{1/6}},\;\; F_{length1}=\exp\left(-3\cdot10^{-2}\left(\tilde{R}e_{\theta t}-460\right)\right)$$

$$Re_{\theta c}=0.67\tilde{R}e_{\theta t}+24\sin\left(\frac{\tilde{R}e_{\theta t}}{240}+0.5\right)+14,\;\; F_{turb}=\left(1-F_{onset}\right)\exp\left(-R_T\right)$$

Regarding the $\tilde{R}e_{\theta t}$ equation, the expression of $F\left(\lambda_\theta\right)$ is

$$F\left(\lambda_\theta\right)_1=1+0.275\left[1-\exp^{\left[-35\lambda_\theta\right]}\right]\exp^{-\frac{Tu}{0.5}},\;\; F\left(\lambda_\theta\right)_2=\phi_{300}\left(F\left(\lambda_\theta\right)_1,1\right)$$

$$F\left(\lambda_\theta\right)_3=1+\left[12.986\lambda_\theta+123.66\lambda_\theta^2+405.689\lambda_\theta^3\right]\exp^{\left[-\left(Tu/1.5\right)^{1.5}\right]}$$

$$F\left(\lambda_\theta\right)=\phi_{-300}\left(F\left(\lambda_\theta\right)_2,F\left(\lambda_\theta\right)_3\right)$$

The coupling with the Spalart-Allmaras model is the same as for the SA-LM2015 model,

$$\tilde{P}_{\tilde{\nu}}=\gamma\rho c_{b_1}\tilde{S}\tilde{\nu},\;\; D_{\tilde{\nu}}=\rho c_{w_1}f_w\left(\frac{\tilde{\nu}}{\Delta}\right)^2$$

1.1.3 The Hamilton--Jacobi Equation

An additional PDE must be solved as part of the system of primal equations. This is the Eikonal or Hamilton--Jacobi equation computing the distance Δ field from the closest solid walls needed for the source terms of the turbulence and transition models. Distances are to be differentiated in the development of the adjoint method and this is why this should be included into the primal equations. This is written as

$$R^\Delta=\frac{\partial}{\partial x_k}\left(\Delta\frac{\partial\Delta}{\partial x_k}\right)-\Delta\frac{\partial}{\partial x_k}\left(\frac{\partial\Delta}{\partial x_k}\right)-1=0 \quad (1.1.8)$$

1.2 Boundary Conditions

Along the solid walls, the no-slip condition $v_k = 0$ is applied. For the Spalart-Allmaras turbulence model, $\tilde{\nu} = 0$, for the $k-\omega$ SST model, $k = 0$ and $\omega = \frac{60\tilde{\nu}}{\beta_1 \Delta^2}$, while for the $\gamma - \tilde{Re}_{\theta t}$ transition model $\frac{\partial \gamma}{\partial n} = 0$ and $\frac{\partial \tilde{Re}_{\theta t}}{\partial n} = 0$. Along the inlet boundary, for the mean-flow equations, four (in 3D) quantities are defined and imposed as Dirichlet conditions and one is extrapolated from the domain interior. In the Spalart-Allmaras model, the inlet viscosity ratio $\left(\frac{\nu_t}{\nu}\right)^{IN}$ is specified. In the $k-\omega$ SST model, the inlet viscosity ratio and the turbulence intensity (Tu) are specified whereas $k^{IN} = 1.5Tu^2 \left|\mathbf{U}\right|^2$ and $\omega^{IN} = k/\nu_t$. For the $\gamma - \tilde{Re}_{\theta t}$ transition model, $\gamma^{IN} = 1$ and $\tilde{Re}_{\theta t}$ is computed based on Eq. 1.1.6 . For the outlet boundary, one quantity is imposed as boundary condition and the rest four are extrapolated from the interior domain for the mean-flow equations, while for the turbulence and transition models, zero Neumann boundary conditions are imposed to $\tilde{\nu}, k, \omega, \gamma$ and $\tilde{Re}_{\theta t}$. The farfield boundary is treated as a combination of inlet and outlet, depending on the local velocity.

1.3 Discretization of the Governing Equations and Numerical Solution

PUMA (7) solves the flow and adjoint equations on discretized unstructured/hybrid grids using vertex-centered finite volumes. Inviscid fluxes are discretized based either on a second-order upwind scheme (Roe scheme, (29), or Flux Vector Splitting, (35)) or a central difference scheme, (16), with a blend of second- and fourth-order differences artificial dissipation. All discretization schemes are second-order accurate.PUMA runs on a GPU cluster and employs either the MPI protocol for data communications between GPUs on different computing nodes or the shared on-node memory for memory transactions between GPUs on the same node. High parallel efficiency is achieved by the use of Mixed Precision Arithmetics (MPA) (7). All residuals are computed in double precision, but the memory demanding L.H.S. operators are stored in single precision accuracy.

1.4 Validation of the Primal Solver

Some validation and verification test cases, for the primal solver (with emphasis laid on the transition model), are presented. Code validation/verification refers to the $\gamma - \tilde{Re}_{\theta t}$ transition model (all of its variants) and its coupling with the k–ω SST and the Spalart-Allmaras turbulence models, as explained before. The purpose is to examine the accuracy of the transition models implementation in the PUMA code, (17), in comparison with other computational results and experiments.

Three test cases are considered: a flat-plate, the NLF(1)--0416 isolated airfoil and the NLF(2)--0415 infinite swept wing. The flat plate and the NLF(1)--0416 case are validated using all transition models (SST-2003-LM2015, SA-noft2-Gamma-Retheta, SA-LM2015 and SA-sLM2015). The investigation of the NLF(2)--0415 swept wing focuses on crossflow instabilities due to surface roughness.

1.4.1 Flat-Plate Test Case

The Schubauer and Klebanoff (30) flat plate experiment is a useful validation test case for transition models. The case has a low freestream turbulence intensity and corresponds to natural transition. A computational grid of $\sim 17K$ nodes is used. The inlet boundary conditions are summarized in Table 1. The non-dimensional first wall distance is $y^+ < 1$.

The skin friction coefficient along the flat plate is compared with experimental data and, also, numerical results obtained by Langtry $\&$ Menter (19) (for the k–ω SST), Fig. 1. A very good agreement with the experimental data is obtained for all transition variants.

Quantity	S&K
Velocity $(\mathrm{m\,s^{-1}})$	50.1
Turbulence Intensity (%)	0.18
Viscosity Ratio	1
Density $(\mathrm{kg\,m^{-3}})$	1.2
Dynamic Viscosity $(10^{-5}\,\mathrm{kg\,m^{-1}\,s^{-1}})$	1.8

Table 1: *Flat Plate*: Inlet Conditions for the flat-plate case at $0.25\,\mathrm{m}$ upstream of the leading edge.

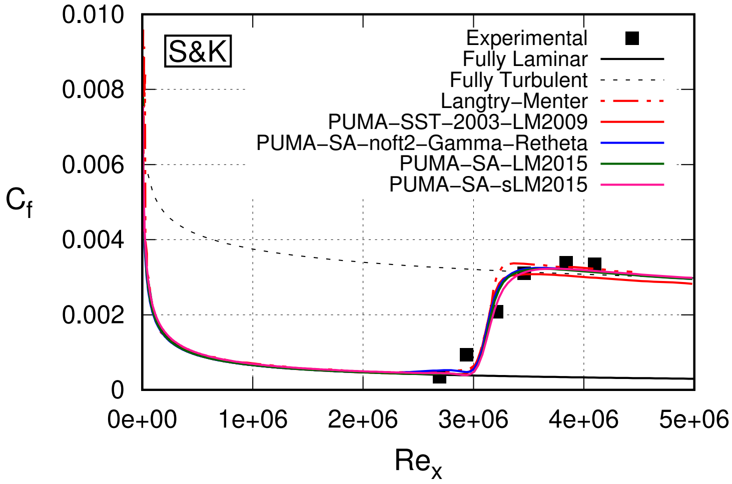

Figure 1: *Flat Plate*: Skin friction coefficient as computed by the programmed add-ons in PUMA for four transition models for the S&K flat plate case compared with experimental (30) and other numerical (19) (labelled as Langtry-Menter) results. Fully laminar and turbulent results are also included.

1.4.2 Flow around the NLF(1)--0416 Airfoil

The NLF(1)--0416 is a low speed Natural Laminar Flow (NLF) airfoil for general aviation applications. The airfoil was tested in various Angles of Attack (AoA) between $-17°$ to $17°$ and experimental data for pressure, lift, drag and momentum coefficient are available in (31). The flow conditions are $Re = 4 \cdot 10^6$, $M_\infty = 0.1$ and $Tu = 0.15\%$. The fine mesh of (11) is used.

The convergence histories of the residuals of the $\gamma - \tilde{Re}_{\theta t}$ transition model variants are presented in Fig. 2 for the fine grid and AoA $= 0°$. Regarding the γ equation, the residuals of the SST-2003-LM2015, SA-noft2-Gamma-Retheta and SA-LM2015 models drop by ~ 3 orders of magnitude while, for the SA-sLM2015, a deep convergence is achieved with a drop of ~ 12 orders of magnitude. The improved numerical behaviour of the SA-sLM2015 model is due to the smooth approximations that replaced the min./max. operators and the conditional statements. A deep convergence of the $\tilde{Re}_{\theta t}$ equation is obtained for all transition models. It should be noted that the comparison of the convergence histories aims at demonstrating the numerical behaviour and robustness of the $\gamma - \tilde{Re}_{\theta t}$ transition model variants; the differences in the convergence rates do not affect the quality of results since all transition models converge, more or less, to the same C_L and C_D values. In view of the adjoint solver, the difference in convergence is significant as the adjoint method requires residuals that vanish. A comparison of their performance against experimental data follows.

Fig. 3 presents the C_L value w.r.t. the AoA, as well as C_L vs C_D polar diagrams for the same four transition models. Results from fully turbulence runs (Spalart-Allmaras and $k-\omega$ SST) are also included. In all cases, the use of transition model improves the quality of the results and a good

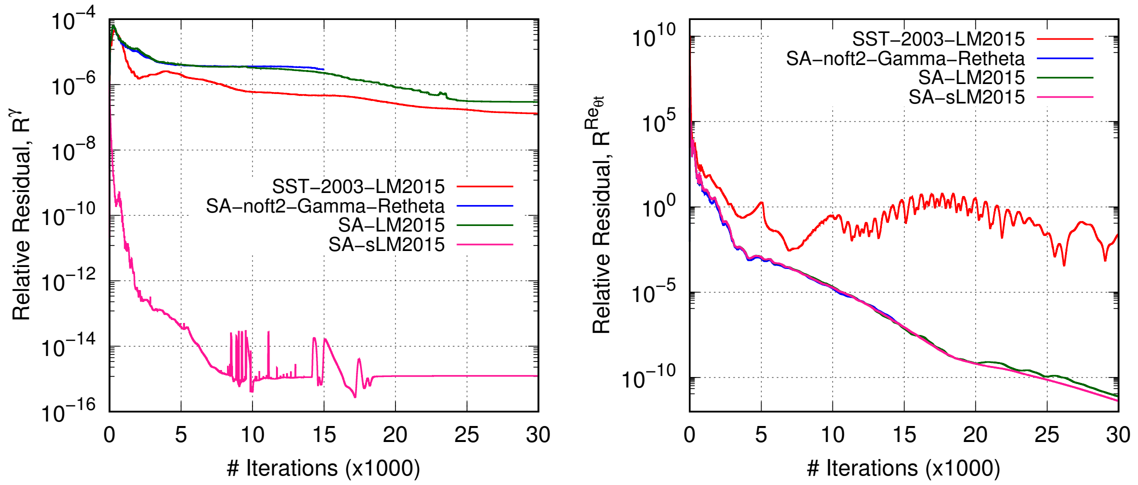

(a) (b)

Figure 2: *NLF(1)--0416 Airfoil*: Relative residual convergence histories for the four transition model on the fine grid and AoA $= 0^{\circ}$. (a) γ and (b) $\tilde{Re}_{\theta t}$ equations.

agreement with the experimental data is achieved. The skin friction coefficient along the airfoil surface, as well as the range of the transition point location (gray area) based on the experimental data, is presented in Fig. 4. It is seen that, all transition models accurately predict the transition location over the suction side, small differences are present over the pressure side where the SST-2003-LM2015 and SA-noft2-Gamma-Retheta models slightly delay the transition onset.

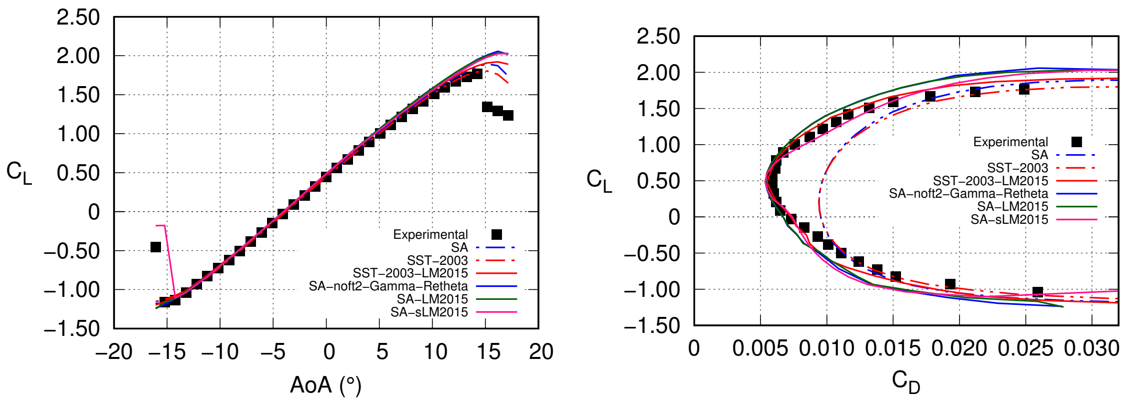

(a) (b)

Figure 3: *NLF(1)--0416 Airfoil*: Comparison of the (a) C_L for several angles of attack and polar diagram (b) (C_L vs C_D). The use of a transition model with both the $k-\omega$ SST and the Spalart-Allmaras turbulence models improves the accuracy of predictions. Results are compared with experimental data (31).

1.4.3 Flow around the NLF(2)--0415 Infinite Swept Wing

For the NLF(2)--0415 infinite swept wing, experiments reported by Dagenhart and Saric, (12), provide data regarding the transition location for $AoA = -4^{\circ}$ and for a wide range of Mach and Reynolds numbers. The simulations performed here are for $M = 0.15$ and $Re = [1.92, 2.19, 2.37, 2.73, 3.27, 3.79] \cdot 10^{6}$, the turbulence intensity level is $Tu = 0.20\%$. The NLF(2)--0415 infinite swept wing consists of the NLF(2)-0415 airfoil extruded with a 45° sweep angle. The grid consists of $\sim 204K$ nodes, three similar

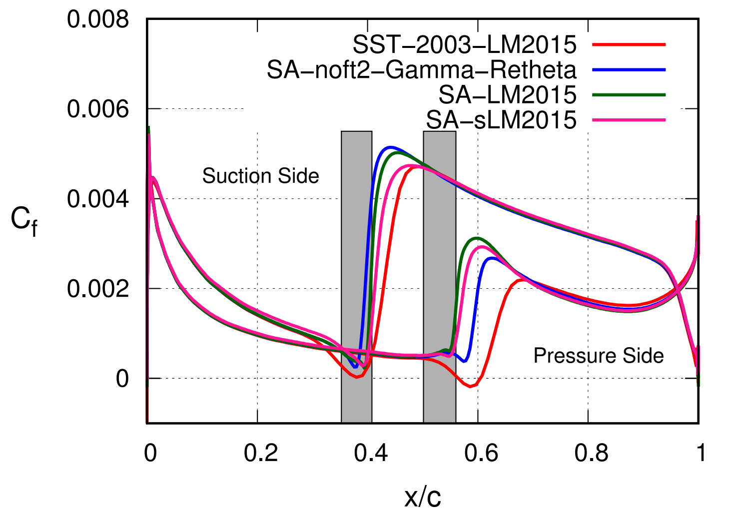

Figure 4: *NLF(1)–0416 Airfoil*: Skin friction coefficient distribution along the pressure and suction sides of the airfoil as computed using PUMA with various transition models, on the fine grid. The area in grey represents the range of the transition location based on the experimental data, (31).

sections are created with $\sim 68K$ nodes each. The maximum y^+ value of the first off the wall nodes is $y^+ = 0.7$. In order to simulate the infinite swept wing, periodic boundaries are imposed.

The transition locations for h_{rms} = 3.3 µm roughness as resulted from the simulations with the SST-2003-LM2015, SA-LM2015 and SA-sLM2015 models are compared with the experimental ((12)) and numerical ((18, 28)) data in Fig. 5. All transition models accurately predict the transition locations for all Reynolds numbers except for the lowest one. This discrepancy is also present in the numerical results of the original models, (28).

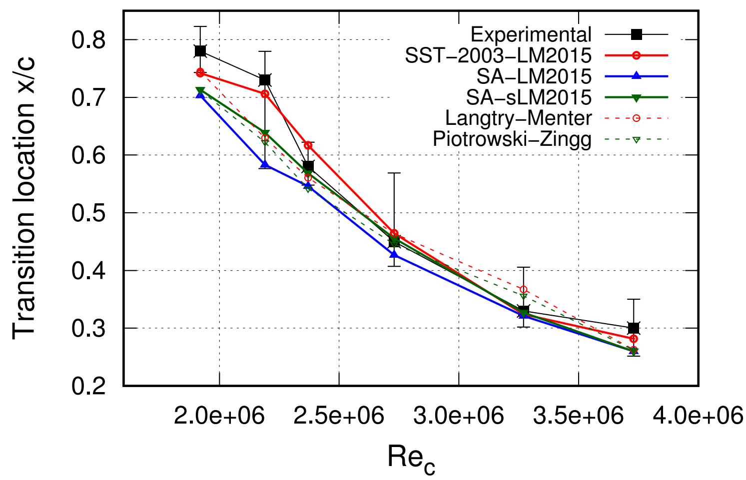

Figure 5: *NLF(2)–0415 Swept Wing*: Comparison of transition location for several Reynolds numbers as computed with PUMA, Langtry&Menter (18) and Piotrowski&Zingg (28) and as exprerimentally measured. (12).

1.5 The Continuous Adjoint Method for Transitional Flows in PUMA

In continuous adjoint, the objective function J is augmented by the field integrals of the product of the primal equations' residuals and the adjoint variables over a finite volume Ω, resulting to the augmented objective function

$$J_{\text{aug}}=J+\int_{\Omega}\Psi_n R_n^{\text{MF}}\mathrm{d}\Omega+\int_{\Omega}\tilde{\nu_a}R^{\tilde{\nu}}\mathrm{d}\Omega+\int_{\Omega}\gamma_a R^{\gamma}\mathrm{d}\Omega+\int_{\Omega}\tilde{Re}_a R^{\tilde{Re}_{\theta t}}\mathrm{d}\Omega+\int_{\Omega}\Delta_a R^{\Delta}\mathrm{d}\Omega \tag{1.5.1}$$

In Eq. 1.5.1 $\Psi_n,(n=1,...,5)$ are the mean-flow adjoint variables (in 3D) and $\tilde{\nu_a}$, γ_a, $\tilde{Re}_a$ and Δ_a are the adjoint Spalart-Allmaras model variable, the adjoint intermittency, the adjoint transition momentum-thickness Reynolds number and the adjoint distance, respectively. The adjoint fields, as extra degrees of freedom, are needed to avoid computing the derivatives of the primal fields w.r.t. the design variables; this is achieved by formulating, discretizing and numerically solving the adjoint equations. Upon convergence of the flow equations $J_{\text{aug}}\equiv J$ and, consequently $\frac{\delta J}{\delta b_i}\equiv\frac{\delta J_{\text{aug}}}{\delta b_i}$ are the sought derivatives. Differentiating J_{aug} w.r.t. the design variables b_i results

$$\frac{\delta J_{\text{aug}}}{\delta b_i}=\frac{\delta J}{\delta b_i}+\underbrace{\int_{\Omega}\Psi_n\frac{\delta R_n}{\delta b_i}\mathrm{d}\Omega}_{\mathcal{I}^{MF}}+\underbrace{\int_{\Omega}\tilde{\nu_a}\frac{\delta R^{\tilde{\nu}}}{\delta b_i}\mathrm{d}\Omega}_{\mathcal{I}^{SA}}+\underbrace{\int_{\Omega}\gamma_a\frac{\delta R^{\gamma}}{\delta b_i}\mathrm{d}\Omega}_{\mathcal{I}^{\gamma}}+\underbrace{\int_{\Omega}\tilde{Re}_a\frac{\delta R^{\tilde{Re}_{\theta t}}}{\delta b_i}\mathrm{d}\Omega}_{\mathcal{I}^{\tilde{Re}_{\theta t}}}+\underbrace{\int_{\Omega}\Delta_a\frac{\delta R^{\Delta}}{\delta b_i}\mathrm{d}\Omega}_{\mathcal{I}^{\Delta}} \tag{1.5.2}$$

Any further development relies on the relationship between the partial ($\frac{\partial}{\partial b_i}$) and total ($\frac{\delta}{\delta b_i}$) derivative of any quantity Φ, given by

$$\frac{\delta\Phi}{\delta b_i}=\frac{\partial\Phi}{\partial b_i}+\frac{\partial\Phi}{\partial x_k}\frac{\delta x_k}{\delta b_i} \tag{1.5.3}$$

where, in the discrete sense, $\frac{\delta x_k}{\delta b_i}$ stand for the grid sensitivities, as well as the expression of the total derivatives of the spatial derivatives of Φ which reads

$$\frac{\delta}{\delta b_i}\left(\frac{\partial\Phi}{\partial x_\ell}\right)=\frac{\partial}{\partial x_\ell}\left(\frac{\delta\Phi}{\delta b_i}\right)-\frac{\partial\Phi}{\partial x_k}\frac{\partial}{\partial x_\ell}\left(\frac{\delta x_k}{\delta b_i}\right) \tag{1.5.4}$$

During the mathematical development of $\frac{\delta J_{\text{aug}}}{\delta b_i}$, volume and surface integrals containing derivatives of the primal variables w.r.t. b_i appear. Setting these multipliers to zero, the so-called field adjoint equations arise. A similar approach is followed for the surface integrals leading to the introduction of the adjoint boundary conditions. Surface or volume integrals which include variation of geometric quantities contribute to the final expression of the sensitivity derivatives.

1.5.1 Field Adjoint Equations and Adjoint Boundary Conditions

Eliminating all volume integrals that contain variations in the mean-flow variables, the Spalart-Allmaras variable, γ, $\tilde{Re}_{\theta t}$ and Δ leads to the mean-flow field adjoint equations, the adjoint Spalart-Allmaras, adjoint $\gamma-\tilde{Re}_{\theta t}$ equations and the adjoint Hamilton-Jacobi equation. The field adjoint equations for transitional flows, (17), read

$$R^{\Psi}_m = -A_{nmk}\frac{\partial \Psi_n}{\partial x_k} - \mathcal{K}_m + \mathcal{K}^{\mathsf{SA}}_m + \mathcal{K}^{\gamma-\tilde{R}e_{\theta t}}_m = 0 \tag{1.5.5 a}$$

$$R^{\tilde{\nu_a}} = -v_k\frac{\partial \tilde{\nu_a}}{\partial x_k} - \mathcal{G}^{\mathsf{SA},diff} + \mathcal{G}^{\mathsf{SA},src} + \left[\mathcal{G}^{\mu_t} + \mathcal{G}^{\mu_t,\gamma-\tilde{R}e_{\theta t}}\right]\frac{\partial \mu_t}{\partial \tilde{\mu}} = 0 \tag{1.5.5 b}$$

$$R^{\gamma_a} = -v_k\frac{\partial \gamma_a}{\partial x_k} - \mathcal{H}^{\gamma-\tilde{R}e_{\theta t},diff}_{\gamma} + \mathcal{H}^{\gamma-\tilde{R}e_{\theta t},src}_{\gamma} + \mathcal{H}^{\mathsf{SA},src}_{\gamma} = 0 \tag{1.5.5 c}$$

$$R^{\tilde{R}e_a} = -v_k\frac{\partial \tilde{R}e_a}{\partial x_k} - \mathcal{H}^{\gamma-\tilde{R}e_{\theta t},diff}_{\tilde{R}e_{\theta t}} + \mathcal{H}^{\gamma-\tilde{R}e_{\theta t},src}_{\tilde{R}e_{\theta t}} + \mathcal{H}^{\mathsf{SA},src}_{\tilde{R}e_{\theta t}} = 0 \tag{1.5.5 d}$$

$$R^{\Delta_a} = -2\frac{\partial}{\partial x_k}\left(\Delta_a\frac{\partial \Delta}{\partial x_k}\right) + \mathcal{M}^{\mathsf{SA},src} + \mathcal{M}^{\gamma-\tilde{R}e_{\theta t},src} = 0 \tag{1.5.5 e}$$

$n = 1,\dots,5$, $m = 1,\dots,5$, $k = 1,\dots,3$ where the terms $\mathcal{K}_m$, $\mathcal{K}^{\mathsf{SA}}_m$ and $\mathcal{K}^{\gamma-\tilde{R}e_{\theta t}}_m$ result from the differentiation of the mean-flow viscous terms and that of the turbulence and transition model. Regarding the field adjoint equation to the Spalart-Allmaras model, $\mathcal{G}^{\mathsf{SA},diff}$ and $\mathcal{G}^{\mathsf{SA},src}$ are from the differentiation of the diffusion and source terms of this model. $\mathcal{G}^{\mu_t}$ and $\mathcal{G}^{\mu_t,\gamma-\tilde{R}e_{\theta t}}$ include the contribution of the mean-flow and $\gamma-\tilde{R}e_{\theta t}$ to μ_t. In the field adjoint equation to the $\gamma-\tilde{R}e_{\theta t}$ model, terms $\mathcal{H}^{\gamma-\tilde{R}e_{\theta t},diff}_{\gamma}/\mathcal{H}^{\gamma-\tilde{R}e_{\theta t},diff}_{\tilde{R}e_{\theta t}}$ $\mathcal{H}^{\gamma-\tilde{R}e_{\theta t},src}_{\gamma}/\mathcal{H}^{\gamma-\tilde{R}e_{\theta t},src}_{\tilde{R}e_{\theta t}}$ and $\mathcal{H}^{\mathsf{SA},src}_{\gamma}/\mathcal{H}^{\mathsf{SA},src}_{\tilde{R}e_{\theta t}}$ are coming from the differentiation of the $\gamma-\tilde{R}e_{\theta t}$ diffusion and source terms and the Spalart-Allmaras source terms. Regarding the adjoint Hamilton--Jacobi equation, terms $\mathcal{M}^{\mathsf{SA},src}$ and $\mathcal{M}^{\gamma-\tilde{R}e_{\theta t},src}$ come from the differentiation of the turbulence and transition model. Terms coming from the differentiation of the transition models differ among each variant.

All volume integrals resulting from the differentiation of J_{aug} were treated giving rise to the field adjoint equations and only the surface integrals remain. These integrals may contain derivatives in geometric quantities w.r.t. b_i or in the flow variables along the boundaries; the former contribute directly to the sensitivity derivatives, while, the latter must be eliminated giving rise to the adjoint boundary conditions. Moreover, the primal flow boundary conditions should be taken into account during this treatment, meaning that the derivatives of all imposed quantities w.r.t. b_i are zero. The remaining flow quantity variations are grouped and their multiplier is set to zero.

1.5.2 Expression of the Sensitivity Derivatives

After satisfying the field adjoint equations and their boundary conditions, the remaining field and surface integrals comprise the formula of the gradient of J. The gradient of J becomes

$$\frac{\delta J}{\delta b_i} = \mathcal{I}^{\mathsf{SD}}_{\mathsf{MF}} + \mathcal{I}^{\mathsf{SD}}_{\mathsf{SA}} + \mathcal{I}^{\mathsf{SD}}_{\gamma-\tilde{R}e_{\theta t}} + \mathcal{I}^{\mathsf{SD}}_{\Delta} \tag{1.5.6}$$

where $\mathcal{I}^{\mathsf{SD}}_{\mathsf{MF}}$, $\mathcal{I}^{\mathsf{SD}}_{\mathsf{SA}}$, $\mathcal{I}^{\mathsf{SD}}_{\gamma-\tilde{R}e_{\theta t}}$ and $\mathcal{I}^{\mathsf{SD}}_{\Delta}$ give below:

$$\begin{aligned}\mathcal{I}^{\mathsf{SD}}_{\mathsf{MF}} = &-\int_{\Omega}\left[\Psi_n\left(\frac{\partial f^{inv}_{nk}}{\partial x_\ell} - \frac{\partial f^{vis}_{nk}}{\partial x_\ell}\right) + \left(\tau^{\mathsf{adj}}_{mk}\frac{\partial v_m}{\partial x_\ell} + q^{\mathsf{adj}}_k\frac{\partial T}{\partial x_\ell}\right)\right]\frac{\partial}{\partial x_k}\left(\frac{\delta x_\ell}{\delta b_i}\right)d\Omega \\ &-\int_{S_{\mathsf{NoSlip}}}\Psi_n\left(f^{\mathsf{inv}}_{nk} - f^{\mathsf{vis}}_{nk}\right)\frac{\delta(\mathsf{n}_k dS)}{\delta b_i} + \int_{S_{\mathsf{NoSlip}}}\Psi_{k+1}p\frac{\delta(\mathsf{n}_k dS)}{\delta b_i} - \int_{S_{\mathsf{NoSlip}}}\Psi_{m+1}\tau_{\ell k}\mathsf{n}_k\mathsf{n}_\ell\frac{\delta(\mathsf{n}_m dS)}{\delta b_i} \\ &-\int_{S_{\mathsf{NoSlip}}}\Psi_{q+1}\mathsf{t}_q\tau_{\ell k}\mathsf{n}_k\mathsf{t}_\ell\mathsf{t}_m\frac{\delta(\mathsf{t}_m dS)}{\delta b_i} + \int_{S_{\mathsf{NoSlip}}}\Psi_{q+1}\mathsf{n}_q\tau_{\ell k}\mathsf{n}_k\mathsf{t}_\ell\mathsf{t}_m\frac{\delta(\mathsf{n}_m dS)}{\delta b_i}\end{aligned}$$

$$
\begin{aligned}
\mathcal{I}_{\text{SA}}^{\text{SD}} = & -\int_{\Omega} \tilde{\nu_a} \frac{\partial \left(\tilde{\mu} v_k\right)}{\partial x_\ell} \frac{\partial}{\partial x_k} \left(\frac{\delta x_\ell}{\delta b_i}\right) d\Omega + \frac{1}{\sigma} \int_{\Omega} \rho \tilde{\nu_a} \frac{\partial}{\partial x_\ell} \left[\left[\nu + (1+c_{b_2}) \tilde{\nu}\right] \frac{\partial \tilde{\nu}}{\partial x_k} \right] \frac{\partial}{\partial x_k} \left(\frac{\delta x_\ell}{\delta b_i}\right) d\Omega \\
& - \frac{1}{\sigma} \int_{\Omega} \frac{\partial \left(\rho \tilde{\nu_a}\right)}{\partial x_k} \left[\nu + (1+c_{b_2}) \tilde{\nu}\right] \frac{\partial \tilde{\nu}}{\partial x_\ell} \frac{\partial}{\partial x_k} \left(\frac{\delta x_\ell}{\delta b_i}\right) d\Omega \\
& + \frac{c_{b2}}{\sigma} \int_{\Omega} \left[\frac{\partial \left(\tilde{\nu_a} \tilde{\mu}\right)}{\partial x_k} \frac{\partial \tilde{\nu}}{\partial x_\ell} - \tilde{\nu_a} \tilde{\mu} \frac{\partial}{\partial x_\ell} \left(\frac{\partial \tilde{\nu}}{\partial x_k}\right) \right] \frac{\partial}{\partial x_k} \left(\frac{\delta x_\ell}{\delta b_i}\right) d\Omega \\
& - \int_{\Omega} \tilde{\nu_a} \frac{\mathcal{C}_{\zeta}^{\text{SA}}}{\zeta} \varepsilon_{k\ell m} \varepsilon_{kqr} \frac{\partial v_r}{\partial x_q} \frac{\partial v_m}{\partial x_p} \frac{\partial}{\partial x_\ell} \left(\frac{\delta x_p}{\delta b_i}\right) d\Omega - \int_{\Omega} \tilde{\nu_a} \frac{\mathcal{C}_{S}^{\text{SA}}}{S} 2 S_{km} \frac{\partial v_k}{\partial x_\ell} \frac{\partial}{\partial x_m} \left(\frac{\delta x_\ell}{\delta b_i}\right) d\Omega \\
& + \frac{1}{\sigma} \int_{S_{\text{NoSlip}}} \rho \tilde{\nu_a} \left[\nu + (1+c_{b_2}) \tilde{\nu}\right] \frac{\partial \tilde{\nu}}{\partial x_k} \frac{\delta \left(\mathsf{n}_k dS\right)}{\delta b_i}
\end{aligned}
$$

$$
\begin{aligned}
\mathcal{I}_{\gamma-\tilde{R}e_{\theta t}}^{\text{SD}} = & -\int_{\Omega} \gamma_a \frac{\partial \left(\rho v_k \gamma\right)}{\partial x_\ell} \frac{\partial}{\partial x_k} \left(\frac{\delta x_\ell}{\delta b_i}\right) d\Omega - \int_{\Omega} \tilde{R}e_a \frac{\partial \left(\rho v_k \tilde{R}e_{\theta t}\right)}{\partial x_\ell} \frac{\partial}{\partial x_k} \left(\frac{\delta x_\ell}{\delta b_i}\right) d\Omega \\
& + \int_{\Omega} \left[\gamma_a \frac{\partial}{\partial x_\ell} \left[\left(\mu + \frac{\mu_t}{\sigma_f}\right) \frac{\partial \gamma}{\partial x_k} \right] - \left(\mu + \frac{\mu_t}{\sigma_f}\right) \frac{\partial \gamma_a}{\partial x_k} \frac{\partial \gamma}{\partial x_\ell} \right] \frac{\partial}{\partial x_k} \left(\frac{\delta x_\ell}{\delta b_i}\right) d\Omega \\
& + \int_{\Omega} \left[\tilde{R}e_a \frac{\partial}{\partial x_\ell} \left[\sigma_{\theta,t} (\mu + \mu_t) \frac{\partial \tilde{R}e_{\theta t}}{\partial x_k} \right] - \sigma_{\theta,t} (\mu + \mu_t) \frac{\partial \tilde{R}e_a}{\partial x_k} \frac{\partial \tilde{R}e_{\theta t}}{\partial x_\ell} \right] \frac{\partial}{\partial x_k} \left(\frac{\delta x_\ell}{\delta b_i}\right) d\Omega \\
& - \int_{\Omega} \tilde{R}e_a \mathcal{C}_{d|\mathbf{U}|ds} \frac{v_k v_m}{|\mathbf{U}|^2} \frac{\partial v_k}{\partial x_\ell} \frac{\partial}{\partial x_m} \left(\frac{\delta x_\ell}{\delta b_i}\right) d\Omega - \int_{\Omega} \frac{\mathcal{C}_{\zeta}^{\gamma-\tilde{R}e_{\theta t}}}{\zeta} \varepsilon_{k\ell m} \varepsilon_{kqr} \frac{\partial v_r}{\partial x_q} \frac{\partial v_m}{\partial x_p} \frac{\partial}{\partial x_\ell} \left(\frac{\delta x_p}{\delta b_i}\right) d\Omega \\
& - \int_{\Omega} \tilde{R}e_a \mathcal{C}_{\zeta_{streamwise}} \frac{v_k}{|\mathbf{U}|} \varepsilon_{kqm} \frac{\partial v_m}{\partial x_\ell} \frac{\partial}{\partial x_q} \left(\frac{\delta x_\ell}{\delta b_i}\right) d\Omega - \int_{\Omega} \frac{\mathcal{C}_{S}^{\gamma-\tilde{R}e_{\theta t}}}{S} 2 S_{km} \frac{\partial v_k}{\partial x_\ell} \frac{\partial}{\partial x_m} \left(\frac{\delta x_\ell}{\delta b_i}\right) d\Omega \\
& + \int_{S_{\text{NoSlip}}} \gamma_a \left(\mu + \frac{\mu_t}{\sigma_f}\right) \frac{\partial \gamma}{\partial x_k} \frac{\delta \left(\mathsf{n}_k dS\right)}{\delta b_i} + \int_{S_{\text{NoSlip}}} \tilde{R}e_a \sigma_{\theta,t} (\mu + \mu_t) \frac{\partial \tilde{R}e_{\theta t}}{\partial x_k} \frac{\delta \left(\mathsf{n}_k dS\right)}{\delta b_i}
\end{aligned}
$$

$$
\mathcal{I}_{\Delta}^{\text{SD}} = -2 \int_{\Omega} \Delta_a \frac{\partial \Delta}{\partial x_k} \frac{\partial \Delta}{\partial x_\ell} \frac{\partial}{\partial x_k} \left(\frac{\delta x_\ell}{\delta b_i}\right) d\Omega
$$

Expression for the rest terms are omitted.

1.6 Verification of the Adjoint Solver and Optimization

In this section, the formulation of the adjoint method for the SA-noft2-Gamma-Retheta, SA-LM2015 and SA-sLM2015 transition models is verified, (17). The NLF(1)--0416 airfoil at AoA $= 2.03°$, extensively validated against experimental data in Sec. 1.4.2, is used. The airfoil is parameterized using the 8×7 NURBS control lattice of Fig. 6, 24 design variables in total. The accuracy of the sensitivity derivatives regarding the drag (C_D) and lift coefficient (C_L) is verified against finite differences which are assumed to give the reference derivatives. The impact of the ``frozen transition'' assumption (according to which the adjoint to the transition model equations is not formulated and solved) is also investigated. The verification of the sensitivity derivatives and the shape optimization of the airfoil are performed with each transition model. The two quantities of interest are expressed as

$$J = \frac{F}{\frac{1}{2}\rho_\infty U_\infty c}, \quad F = \int_{S_{\text{Obj}}} (p\mathrm{n}_k - \tau_{km}\mathrm{n}_m r_k)\, dS$$

where F stands for the aerodynamic force (drag or lift) and r_k is the direction of the force component, for drag $r_k^D = (-\sin\alpha_\infty, \cos\alpha_\infty)$ and lift $r_k^L = (\cos\alpha_\infty, \sin\alpha_\infty)$.

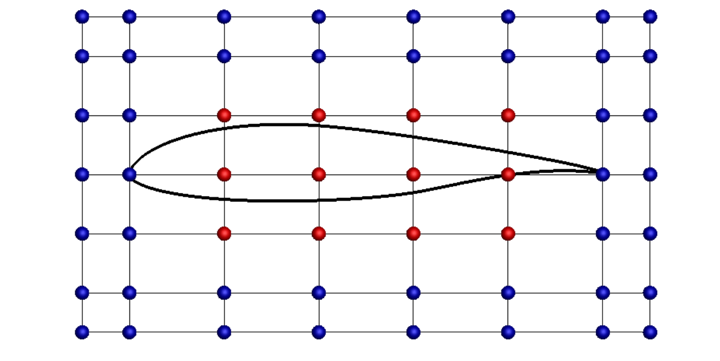

Figure 6: *Optimization of the NLF(1)--0416 Airfoil*: Parameterization of the airfoil. Control points in blue remain constant while red ones are allowed to move in the chordwise and the normal-to-the-chord direction.

The sensitivity derivatives of C_D and C_L computed by the adjoint method, with and without the ``frozen transition'' assumption, are compared with FDs in Figs. 7a, 7b and 7c for the SA-noft2-Gamma-Retheta, the SA-LM2015 and the SA-sLM2015 model, respectively. The first half sensitivity derivatives correspond to the x coordinates and the second half to the y coordinates of the CPs. The adjoint method reproduces the outcome of the finite differences with high accuracy for both C_D and C_L. On the other hand, the ``frozen transition'' assumption is harmful to the gradient accuracy; higher deviations of the ``frozen transition'' sensitivity derivatives can be seen for the C_D sensitivity derivatives, as occasionally they even have the opposite sign (i.e. design variable with ID 21).

After verifying the grdients, the optimization of the NLF(1)--0416 airfoil for min. C_D under the double-sided inequality constraint that C_L remains close to that of the baseline airfoil (should not change by more than $\pm 1\%$), is carried out. An additional inequality constraint, requiring that the airfoil area should not drop below 90% of the baseline one is imposed. The optimization is performed three times, once for each transition model variant; the convergence histories are plotted in Fig. 8. The optimizations based on the SA-noft2-Gamma-Retheta, the SA-LM2015 and SA-sLM2015 models resulted to $\sim 7.5\%$, $\sim 17.4\%$ and $\sim 28.7\%$ reduction of the C_D value, respectively, maintaining the C_L close to the baseline one by $\pm 1\%$. The volumes (areas) of the optimized airfoils reduce by 10%, reaching the minimum allowed value of the constraint value. It seems that the optimization runs based on the SA-noft2-Gamma-Retheta and the SA-LM2015 transition models have been trapped into local minima, in the sense that there are several airfoils with the same target values, meeting the imposed contraint.

The geometry and the skin friction coefficient distribution for the baseline and the three optimized airfoils are presented in Fig. 9. All optimization runs resulted to an airfoil geometry with almost flat pressure side, Fig. 9a. Differences are located at the suction side, where the optimization relying on the SA-sLM2015 model increased and shifted the curvature to the trailing edge. These are reflected on the skin friction distribution of the optimized airfoils. Regarding the optimization on the SA-noft2-Gamma-Retheta model, there is a slight change in the C_f distribution, Fig. 9b. Regarding the optimizations based on the SA-LM2015 and SA-sLM2015 models, Figs. 9c and 9d, the transition location on the pressure side is more or less the same for the two airfoils, shifted by $\sim 20\%$ chord downstream. On

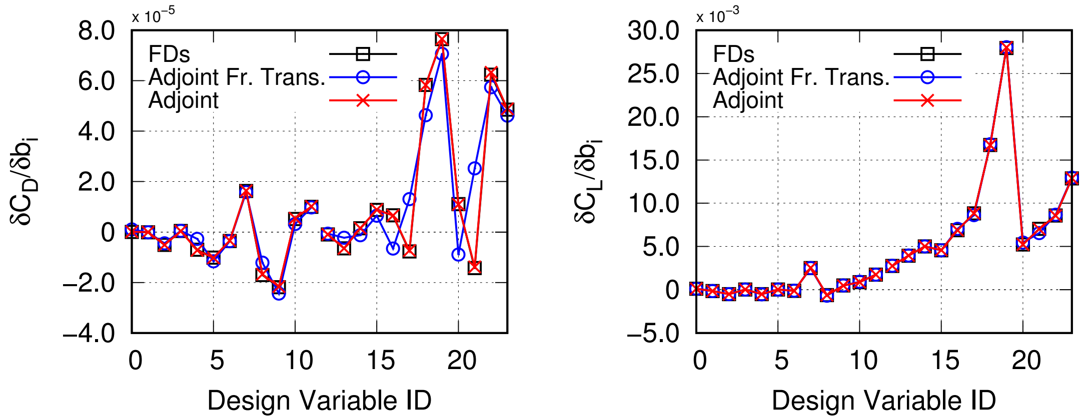

(a) SA-noft2-Gamma-Retheta

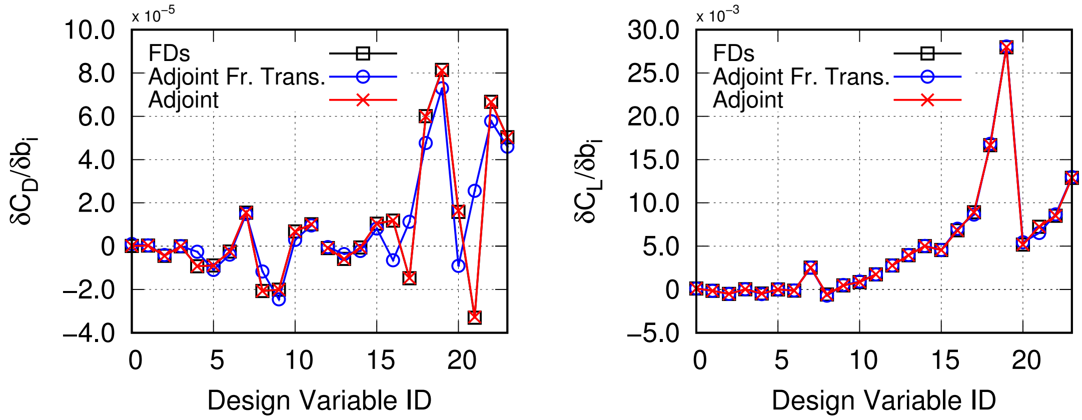

(b) SA-LM2015

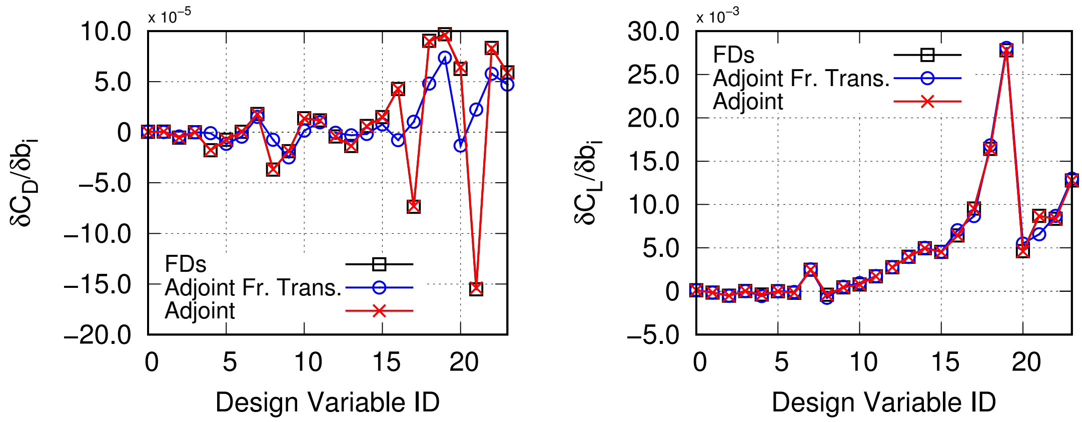

(c) SA-sLM2015

Figure 7: *Optimization of the NLF(1)–0416 Airfoil*: Comparison of the C_D (left) and C_L (right) sensitivity derivatives computed by the continuous adjoint method, with and without the ``frozen transition'' assumption, with finite differences (FDs). Derivatives based on the (a) SA-noft2-Gamma-Retheta, (b) SA-LM2015 and (c) SA-sLM2015 transition models.

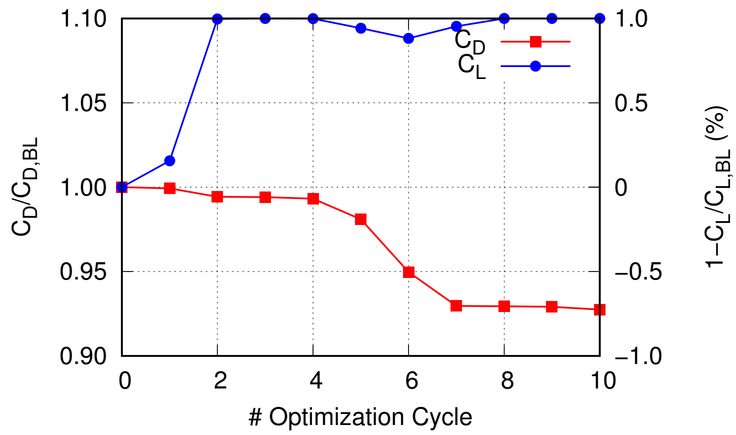

(a) SA-noft2-Gamma-Retheta

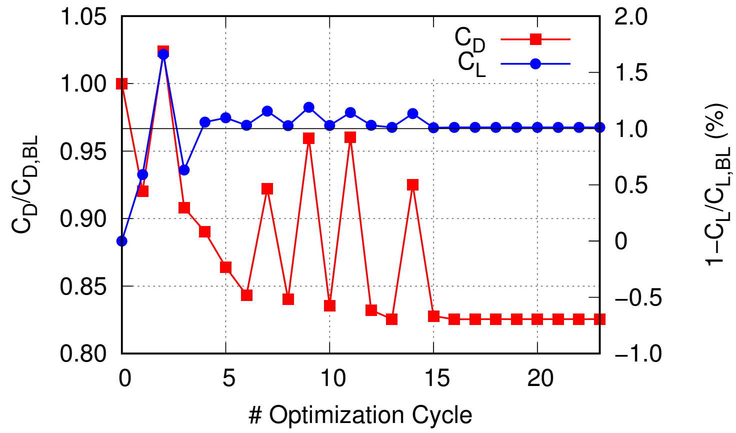

(b) SA-LM2015

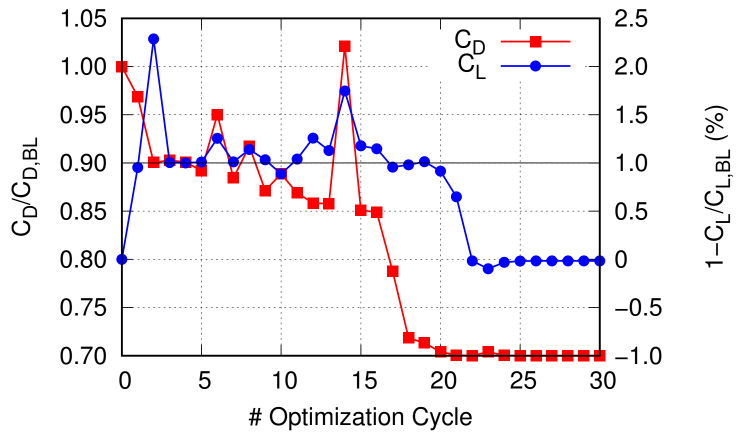

(c) SA-sLM2015

Figure 8: *Optimization of the NLF(1)–0416 Airfoil*: Evolution of the objective (C_D) and constraint (C_L) functions during optimizations based on (a) SA-noft2-Gamma-Retheta, (b) SA-LM2015 and (c) SA-sLM2015 transition model.

the other hand, transition locations over the suction side differ; the optimized geometry based on the SA-sLM2015 model has the largest shift ($\sim 17\%$ chord) leading to a greater C_D reduction.

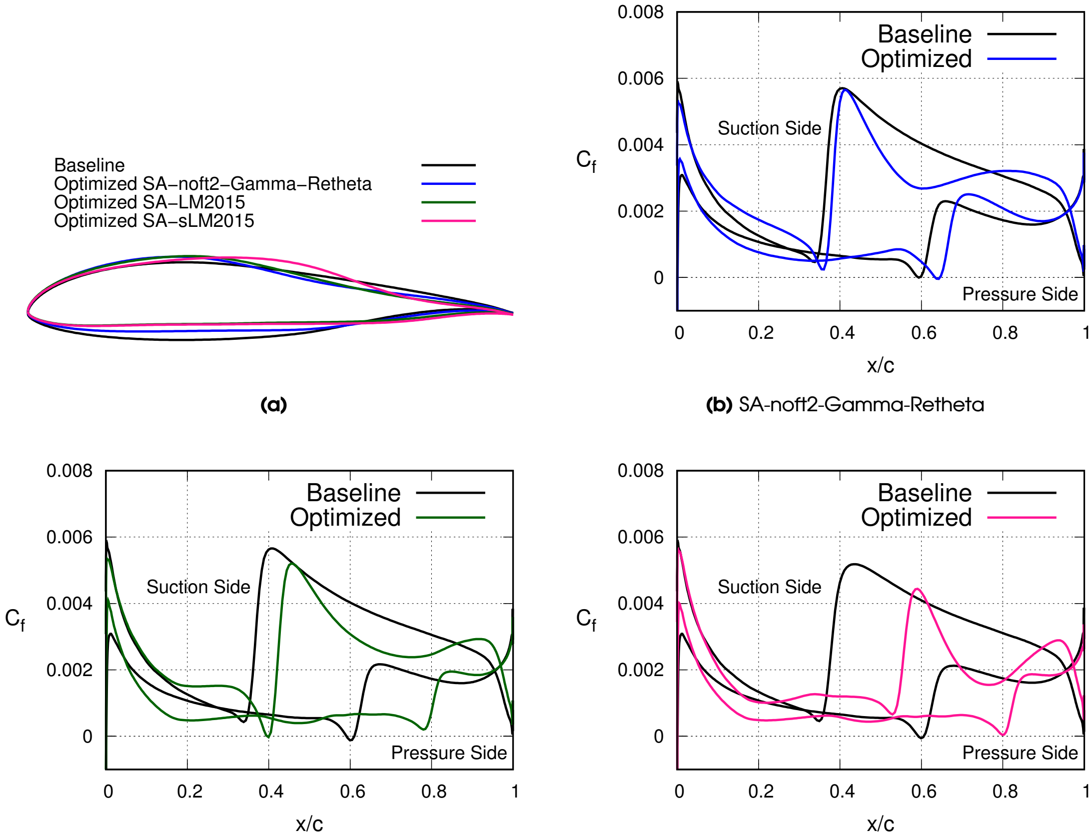

(a) **(b)** SA-noft2-Gamma-Retheta

(c) SA-LM2015 **(d)** SA-sLM2015

Figure 9: *Optimization of the NLF(1)--0416 Airfoil*: (a) Baseline and optimized airfoil geometries. Skin friction coefficient distribution along the airfoil surface for the baseline and the optimized with the (b) SA-noft2-Gamma-Retheta, (c) SA-LM2015 and (d) SA-sLM2015 transition models geometries.

2 Contributions by INRIA

2.1 Vector form of the RANS Equations

The RANS equations can be rewritten in the following differential form:

$$W_t + \nabla \cdot (\mathcal{F}^E - \mathcal{F}^V) = 0\,, \tag{2.1.1}$$

where W is the vector of conservative variables

$$W = (\rho, \rho u, \rho v, \rho w, \rho E)^T \;,$$

while $\mathcal{F}^E$ and $\mathcal{F}^V$ are the convective and the viscous flux vector, respectively defined as

$$\begin{aligned} \mathcal{F}^E(W) &= (\rho\,\mathbf{u},\ \rho u\,\mathbf{u} + p\mathbf{e}_1,\ \rho v\,\mathbf{u} + p\mathbf{e}_2,\ \rho w\,\mathbf{u} + p\mathbf{e}_3,\ \mathbf{u}(\rho E + p))^T \;, \\ \mathcal{F}^V(W) &= (0,\ \mathcal{T}_1,\ \mathcal{T}_2,\ \mathcal{T}_3,\ \mathcal{T}\cdot\mathbf{u} + (\lambda + \lambda_t)\nabla T)^T \end{aligned} \tag{2.1.2}$$

with $(\mathbf{e}_1, \mathbf{e}_2, \mathbf{e}_3)$ the Cartesian coordinate directions unit vectors.

The physical variables of the problem are the density ρ, the velocity $\mathbf{u}$, the static pressure p and the total specific energy E. The latter is defined as the sum of the flow specific internal energy e and the specific kinetic one as

$$E = e + \frac{\|\mathbf{u}\|^2}{2}\,.$$

The fluid is assumed to be Newtonian and, via the *Boussinesq* hypothesis, the stress tensor $\mathcal{T}$ is defined by

$$\mathcal{T} = 2\,(\mu + \mu_t)\left[\frac{1}{2}(\nabla\mathbf{u} + (\nabla\mathbf{u})^T) - \frac{1}{3}(\nabla\cdot\mathbf{u})\,\mathbb{I}\right], \tag{2.1.3}$$

where μ denotes the molecular dynamic viscosity which, for a perfect gas is usually imposed to obey Sutherland's law i.e.,

$$\mu \;=\; \mu_\infty \left(\frac{T}{T_\infty}\right)^{\frac{3}{2}} \left(\frac{T_\infty + \mathrm{Su}}{T + \mathrm{Su}}\right).$$

$\mathrm{Su} = 110.4\,\mathrm{K}$ is the Sutherland temperature for dry air and the index ∞ denotes reference quantities.

λ stands for the thermal conductivity coefficient and T for the absolute static temperature. In the case of gases, λ (resp. λ_t) depends on temperature in a similar way as μ (resp. μ_t). For this reason, the following relationships are accepted

$$\lambda = c_p\frac{\mu}{\mathrm{Pr}} \qquad \text{and} \qquad \lambda_t = c_p\frac{\mu_t}{\mathrm{Pr}_t}$$

with $\mathrm{Pr} = 0.72$ and $\mathrm{Pr}_t = 0.9$ for (dry) air.

Assuming the fluid to be a calorically perfect gas,

$$p = \rho R T, \qquad e = c_v T \tag{2.1.4}$$

where $R = \mathcal{R}/M$ is the perfect gas constant divided by the molar mass of the fluid, commonly set at $287.1\,\mathrm{J\,kg^{-1}\,K^{-1}}$ for air and c_v is the specific heat capacity at constant volume. The latter is linked to specific heat capacity at constant pressure c_p by the specific heat ratio $\gamma = c_p/c_v$, set at 1.4 for diatomic gas.

In order to close the system, μ_t is calculated by means of a turbulence model.

Turbulence modeling: Negative Spalart-Allmaras One-Equation Model without ft2 Term (SA-neg-noft2)
The turbulence formulation considered here is the Negative Spalart-Allmaras turbulence model with neglecting trip terms (SA-neg-noft2) (33). It consists of a convection-diffusion equation for the pseudo turbulent viscosity variable $\widetilde{\nu}$ where the source term is obtained as a balance between a production term and a destruction term associated with the same quantity. Specifically, when $\tilde{\nu}$ is greater than or equal to zero, the equation consists in

$$\frac{\partial \rho\tilde{\nu}}{\partial t} + \underbrace{\nabla \cdot (\rho \mathbf{u} \tilde{\nu})}_{convection} - \underbrace{\frac{\rho}{\sigma}\nabla \cdot ((\nu + \tilde{\nu})\nabla\tilde{\nu})}_{dissipation} = \underbrace{\frac{c_{b2}\rho}{\sigma}\|\nabla\tilde{\nu}\|^2}_{diffusion} + \underbrace{c_{b1}\tilde{S}\rho\tilde{\nu}}_{production} - \underbrace{c_{w1} f_w \rho \left(\frac{\tilde{\nu}}{d}\right)^2}_{destruction} .$$

On the other hand, when $\tilde{\nu}$ is negative the following equation is solved instead

$$\frac{\partial \rho\tilde{\nu}}{\partial t} + \nabla \cdot (\rho \mathbf{u} \tilde{\nu}) - \frac{\rho}{\sigma}\nabla \cdot ((\nu + f_n\tilde{\nu})\nabla\tilde{\nu}) = \frac{c_{b2}\rho}{\sigma}\|\nabla\tilde{\nu}\|^2 + c_{b1}\rho\|\nabla \times \mathbf{u}\| - c_{w1}\rho \left(\frac{\tilde{\nu}}{d}\right)^2$$

with

$$f_n = \frac{16 + \chi^3}{16 - \chi^3} .$$

The turbulent viscosity is computed from:

$$\mu_t = \rho\tilde{\nu} f_{v1} ,$$

where

$$f_{v1} = \frac{\chi^3}{\chi^3 + c_{v1}^3} \quad \text{and} \quad \chi = \frac{\tilde{\nu}}{\nu} \quad \text{with} \quad \nu = \frac{\mu}{\rho} .$$

Additional definitions are given by the following equations:

$$f_{v2} = 1 - \frac{\chi}{1 + \chi f_{v1}} \quad \text{and} \quad \tilde{S} = \|\nabla \times \mathbf{u}\| + \frac{\tilde{\nu}}{\kappa^2 d^2} f_{v2}$$

where d is the distance to nearest wall which is computed for each vertex at the beginning of the simulation. The set of closure constants for the model is given by

$$\begin{aligned} &\sigma = 2/3 , & &c_{b1} = 0.1355 , & &c_{b2} = 0.622 , & &\kappa = 0.41 , \\ &c_{w1} = c_{b1}/\kappa^2 + (1 + c_{b2})/\sigma , & &c_{w2} = 0.3 , & &c_{w3} = 2 , & &c_{v1} = 7.1 . \end{aligned}$$

Finally, the function f_w is computed as:

$$f_w = g\left(\frac{1 + c_{w3}^6}{g^6 + c_{w3}^6}\right)^{1/6} \quad \text{with} \quad g = r + c_{w2}\left(r^6 - r\right) \quad \text{and} \quad r = \min\left(\frac{\tilde{\nu}}{\tilde{S}\kappa^2 d^2}, 10\right) .$$

Transitional model: Spalart-Allmaras 1-equation BCM Transitional Model (SA-neg-noft2-BCM) (9)
The transitional model considered in this work relies on a modification of the production term of the SA-neg-noft2, which is multiplied with a γ_{BC} intermittency function. This function damps any turbulence production until some transition criteria is achieved, as

$$\frac{\partial \rho\tilde{\nu}}{\partial t} + \nabla\cdot(\rho\mathbf{u}\tilde{\nu}) - \frac{\rho}{\sigma}\nabla\cdot((\nu+\tilde{\nu})\nabla\tilde{\nu}) = \frac{c_{b2}\rho}{\sigma}\|\nabla\tilde{\nu}\|^2 + c_{b1}\gamma_{BC}\tilde{S}\rho\tilde{\nu} - c_{w1}f_w\rho\left(\frac{\tilde{\nu}}{d}\right)^2 \qquad \tilde{\nu} > 0$$

$$\frac{\partial \rho\tilde{\nu}}{\partial t} + \nabla\cdot(\rho\mathbf{u}\tilde{\nu}) - \frac{\rho}{\sigma}\nabla\cdot((\nu+f_n\tilde{\nu})\nabla\tilde{\nu}) = \frac{c_{b2}\rho}{\sigma}\|\nabla\tilde{\nu}\|^2 + c_{b1}\gamma_{BC}\rho\|\nabla\times\mathbf{u}\| + c_{w1}\rho\left(\frac{\tilde{\nu}}{d}\right)^2 \qquad \tilde{\nu} < 0$$

with

$$\gamma_{BC} = 1 - \exp\left(-\sqrt{T_1} - \sqrt{T_2}\right).$$

T_1 and T_2 are triggering functions defined as

$$T_1 = \frac{\max\left(Re_\theta - Re_{\theta,c}, 0.\right)}{\chi_1 Re_{\theta,c}}, \quad T_2 = \max\left(\frac{\mu_T}{\chi_2\mu}, 0.\right),$$

with $\chi_1 = 0.002$ and $\chi_2 = 0.02$.

The transition onset is based on the following experimental correlation

$$Re_{\theta,c} = 803.73\left(Tu_\infty + 0.6067\right)^{-1.027},$$

where Tu_∞ is the free-stream turbulence intensity and Re_θ is based on

$$Re_\theta = \frac{Re_v}{2.193}, \qquad Re_v = \frac{\rho\, d^2\,\|\nabla\times\mathbf{u}\|}{\mu}.$$

The free-stream boundary condition is

$$\frac{\tilde{\nu}_\infty}{\nu_\infty} = 0.02.$$

Pay attention to the fact that turbulence intensity must be specified in percent i.e., if it is about 0.18% you need to set $Tu_\infty = 0.18$.

2.2 RANS flow solver

The Reynolds-Averaged Navier-Stokes (RANS) numerical simulations with the Spalart-Allmaras turbulence model coupled with BCM transitional model (SA-neg-noft2-BCM) are considered here. The code used for all simulations is Wolf, which is a vertex-centered (flow variables are stored at vertices of the mesh) mixed Finite Volume - Finite Element solver on unstructured meshes composed of triangles in 2D and tetrahedra in 3D (3, 25, 1, 2). This means that the convective terms are solved by the Finite Volume method on a dual mesh composed of median cells, while the viscous fluxes are evaluated using the Finite Element method (1, 2). The time integration considers an implicit temporal discretization. Particularly, at each time step the RANS system of equations is approximately solved using a Symmetric Gauss-Seidel (SGS) implicit solver, and local time stepping with local CFL is used to accelerate the convergence to steady state. An implicit loosely coupled algorithm is used to integrate the mean-flow equations and Spalart-Allmaras turbulence equation separately.

2.3 Mesh adaptation

In the mesh adaptation process, the local size and anisotropy of the mesh are prescribed using a metric field (4, 2). A tetrahedron is said *unit* according to a metric if all its edges have unit length in this metric. Similarly, a unit mesh, for a given metric field, is a mesh composed of unit elements in this metric. This establishes a duality between meshes and metrics: a Riemannian metric field can be seen as the continuous counterpart of a mesh. This framework is developed more extensively in (20, 21). In this way, the mesh generation procedure is recasted in generating a uniform unit mesh in the prescribed metric space.

Denoting by $\mathcal{M}_{\text{Opt}}$ the optimal metric, $\mathcal{C}(\mathcal{M}_{\text{Opt}})$ its complexity, *i.e.* the continuous counterpart to mesh size, $\mathcal{N}$ a target complexity, and $\mathcal{E}$ the error model for the considered application, the problem to solve is

$$\mathcal{M}_{\text{Opt}} = \underset{\mathcal{C}(\mathcal{M})=\mathcal{N}}{\text{argmin}}\ \mathcal{E}(\mathcal{M}).$$

This non-linear process is depicted in Algorithm 1. The optimal metric field $\mathcal{M}_{\text{Opt}}$ used to prescribe the new adapted mesh $\mathcal{H}$ is automatically deduced from the actual solution or from the actual solution and adjoint state with different error estimates (2). In practice, an additional step is required between the metric computation step and the mesh generation step, called metric gradation. Indeed, metrics computed from numerical solutions are likely to show irregularities and need to be smoothed, through a gradation process, to improve the quality of the adapted mesh (8, 6).

Algorithm 1: General mesh adaptation loop with mesh-convergence analysis

Input: Initial mesh $\mathcal{H}_0^0$, solution W_0^0, and complexity $\mathcal{C}^0$

while ($\mathcal{C}^j <= \mathcal{C}^{\text{max}}$) **do**

Inner loop to converge the mesh adaptation at fixed complexity:

1. **while** ($i \leq n_{\text{adap}}$) **do**

    (a) Compute the optimal metric for the considered error estimate and complexity $\rightarrow \mathcal{M}_{i-1}^{j,0}$;

    (b) Apply a gradation correction to smooth the metric field $\rightarrow \mathcal{M}_{i-1}^{j}$;

    (c) Generate a new adapted mesh $\rightarrow \mathcal{H}_i^j$;

    (d) Interpolate the solution on the new mesh $\rightarrow (W^0)_i^j$;

    (e) Compute the solution $\rightarrow W_i^j$

    (f) **if** (Convergence check) **then** the loop has converged

    $i = n_{\text{adap}} + 1$;

    else the loop has not converged

    $i = i + 1$;

    end

   end

2. $\mathcal{H}_0^{j+1} = \mathcal{H}_{n_{\text{adap}}}^j$; $W_0^{j+1} = W_{n_{\text{adap}}}^j$; $\mathcal{C}^{j+1} = \alpha \cdot \mathcal{C}^j$;

end

Error estimate The flow solver Wolf can provide metrics for either *feature-based* or *goal-oriented* error estimates. *Feature-based* adaptation aims at minimizing the interpolation error in L^p norm of a given sensor for a given number of degrees of freedom. It is easy to implements as it only requires the second derivatives of the sensor. The *goal-oriented* error estimate minimizes the error of a given engineering output functional for a given number of degrees of freedom. It is more complex because requires a robust adjoint solver and a proper differentiation of the output functionals (2).

The objective of our study is the assessment of an anisotropic mesh-converged solution for the SA-neg-noft2-BCM transitional model. The mesh adaptation process is performed using the mesh-adaptive solution platform composed of Wolf, the anisotropic local remeshing software Feflo.a (22, 23, 24) and the field interpolator Interpol (5).

Two cases are considered.

- 2D Zero-Pressure-Gradient Flat Plate run with the a featured-based (FB) error estimator;
- 2D subsonic flow past the NLF4016 airfoil run with the a goal-oriented (GO) error estimator.

2.4 2D Zero-Pressure-Gradient Flat Plate

The first test case considered is the subsonic flow over a 2D flat plate with zero pressure gradient. The flow conditions are: Mach number $M = 0.1443$ and Reynolds number $Re = 3.34 \times 10^6$, with the latter based on the unit flat plate length. The Turbulence Intensity specified at free-stream is $Tu_\infty = 0.18\%$. This case corresponds to the Schubauer and Klebanoff (30) and was already used to calibrate the BCM-model (27). The FB error estimator considered is based on the L^4 norm of the interpolation error of the local Mach number.

2.4.1 Assessment of an anisotropic metric-based mesh-converged solution with FB error estimator

Figure 10 shows on the left, from a 500-vertices to a $80\,000$-vertices adapted mesh: (i) the mesh-convergence of the drag coefficient C_D for the fully turbulent calculation (blue curve); (ii) the mesh-convergence of the drag coefficient C_D for the transitional calculation (red curve).

First, the fully turbulent RANS adaptive process is performed. Second, the solution computed on a 2000-vertices adapted mesh is used to initialize the transitional calculation. We can see that both calculations are converged at $20\,000$ vertices. Figure 10 on the right shows the comparison between the two Skin Friction coefficients on a $20\,000$ adapted mesh. Transition occurs shortly before $Re_x = 3 \times 10^6$, according to literature.

2.4.2 Transition point mesh-convergence

Our main objective was to assess mesh-convergence solution for the BCM-model, specifically in terms of the position of the transition point. Figure 10 on the right, shows that during the adaptation process, the transition point does not oscillate but converge to a specific position. This means that this model is robust and guarantees mesh-convergence solutions. Particularly, the reader can note that the transition points does not change anymore since $20\,000$ vertices.

The resulting adapted meshes are shown in Figure 11. On the left, adapted mesh and solution for the SA model. On the right, adapted mesh and solution for the SA-BCM model. Both meshes are stretched along the wall-normal direction by a factor 20, to highlight the leading edge and the transitional region. We can see that the adaptation process captures automatically all discontinuities in the flow. Specifically, the leading edge is a discontinuity in terms of boundary condition. The transition point is a discontinuity in the solution, when passing from laminar to turbulent flow.

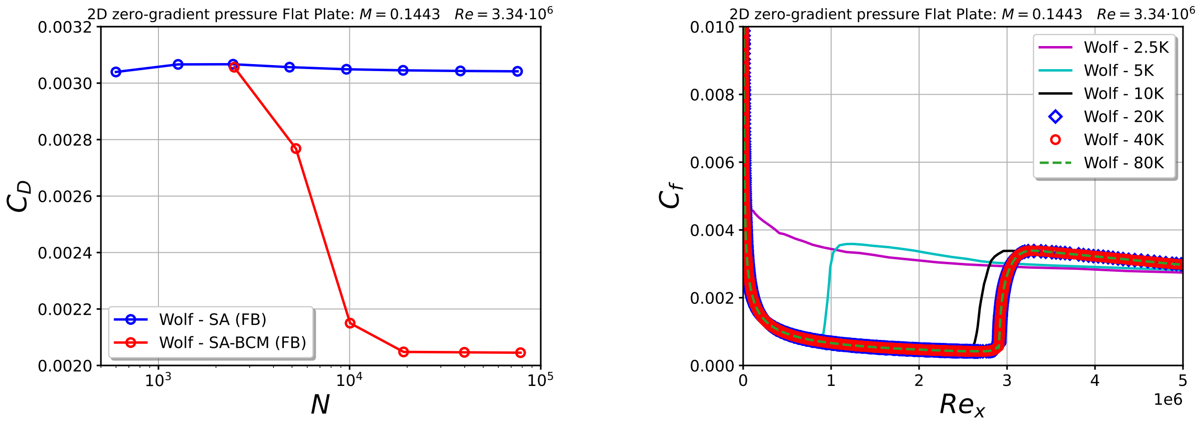

Figure 10: 2D Zero-Pressure-Gradient Flat Plate FB anisotropic metric-based mesh adaptation. (left) Evolution of the Drag C_D coefficient during the mesh-convergence process. N is the number of vertices of the adapted meshes. (right) Skin Friction C_f coefficient on a $20\,000$ vertices-adapted meshes. Comparison between fully turbulent calculation and transitional calculation.

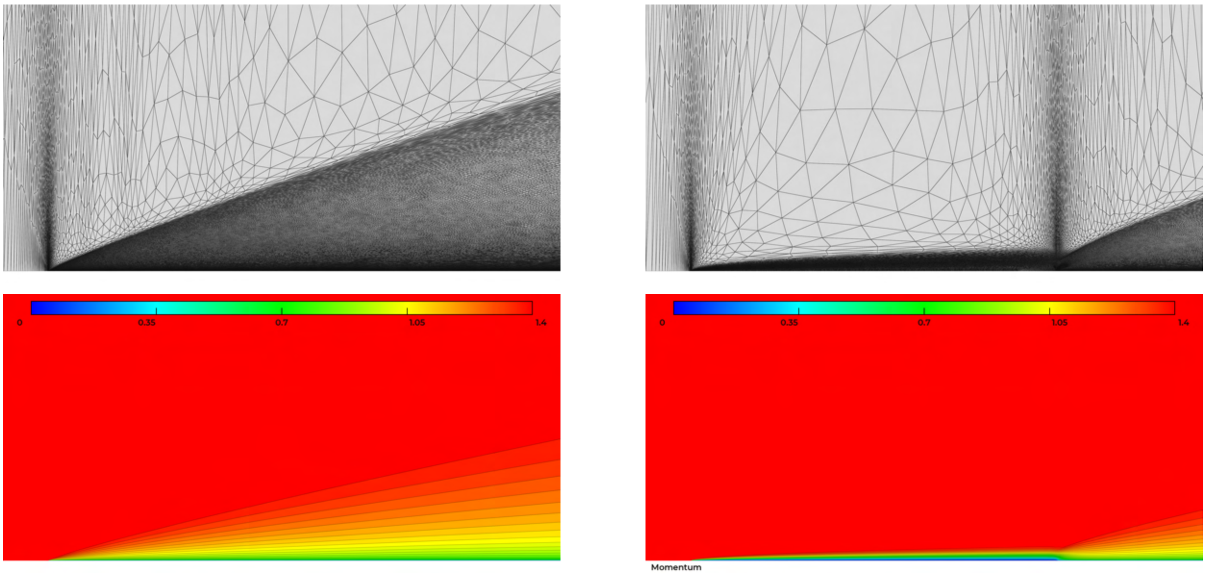

Figure 11: 2D Zero-Pressure-Gradient Flat Plate FB anisotropic metric-based mesh adaptation. (left) Adapted mesh and streamwise velocity component field for turbulent solution. (right) Adapted mesh for and streamwise velocity component field for transitional solution. Both meshes are stretched along the wall-normal direction by a factor 20, to highlight the leading edge and the transitional region.

A zoom of the transition point is shown in Figure 12. Both meshes are stretched along the wall-normal direction by a factor 5, to highlight the refinement at the transition point. We can see in detail as the adaptation process dispenses the proper number of points according to the complexity of the flow. The laminar boundary layer requires much less points w.r.t. the turbulent one, to be correctly captured. Then, we can see the transition to turbulence already in the mesh: the upstream region for the SA-BCM calculation is laminar, velocity gradients are lower and boundary layer is thin. Downstream, velocity gradients are higher and boundary layer is thick. Such physical considerations are well highlighted by the refinement region. In the transition region, adaptation become more isotropic to capture transition. While being highly anisotropic before and after the transition region.

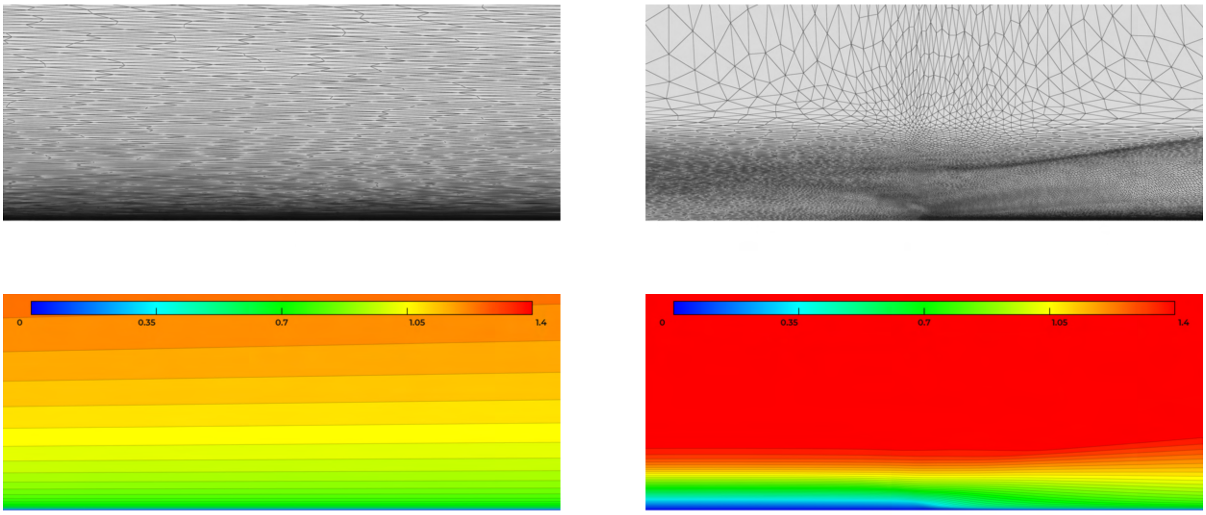

Figure 12: 2D Zero-Pressure-Gradient Flat Plate FB anisotropic metric-based mesh adaptation. (left) Adapted mesh for turbulent solution. (right) Adapted mesh for transitional solution. Both meshes are stretched along the wall-normal direction by a factor 5, to the transitional region.

2.5 2D subsonic flow past the NLF4016 airfoil

The case considered is the flow around the NLF4016 airfoil at Mach number $M = 0.1$ and Reynolds number $Re = 4 \times 10^6$ based on the airfoil chord length c. Several experimental data are available for Re ranging from 1×10^6 to 9×10^6, and M from 0.1 to 0.4 (32). In these experiments a specific roughness was opportunely sized for each Reynolds number to fix the transition point at $0.075c$ on both surfaces.

2.5.1 Assessment of an anisotropic metric-based mesh-converged solution with GO error estimator

The NLF4016 airfoil is run with the goal-oriented error estimator using the drag as the targeted functional.

The SA-BCM model, with fixed free-stream turbulence intensity Tu_∞ is used to calculate the adapted RANS solution. The free-stream temperature is set at $T_\infty = 300\,\mathrm{K}$ and the free-stream Turbulence Intensity at $Tu_\infty = 0.15\,\%$, according to the 1st AIAA Transition Modeling Workshop. However, it should be stressed that an-induced transition by roughness is totally different by a by-pass one induced by a fixed free-stream turbulence. Therefore there is no guarantee that the transition point is the same as that measured in the experiments.

As previously done for the 2D flate plate calculation, the adaptive process for the SA-BCM model is initialized with a corresponding SA adapted solution at $10\,000$ vertices. The process is stopped when reaching a $300\,000$ vertices adapted mesh. A polar from $0°$ to $5°$ Angle of Attack each $1°$ is investigated. The mesh and the solution, for AoA = $0°$ at $30\,000$ vertices for the SA and the SA-BCM model are shown in Figure 13. We can see that also in this case, the adaptive process manages to adapt the mesh to the transition from laminar to turbulent flow.

The drag coefficient C_D evolution of SA and $SA - BCM$ calculations during the adaptive process is shown in Figure 14. We can see that both calculations are mesh-converged at $150\,000$ vertices.

2.5.2 Transition point mesh-convergence

Figure 15 shows the convergence of the transition point during the adaptation process. As for the 2D flat plate, the transition point converges to a specific location and it does not change anymore since the $150\,000$ vertices-adapted mesh. This mesh-convergence is achieved for all the AoAs investigated.

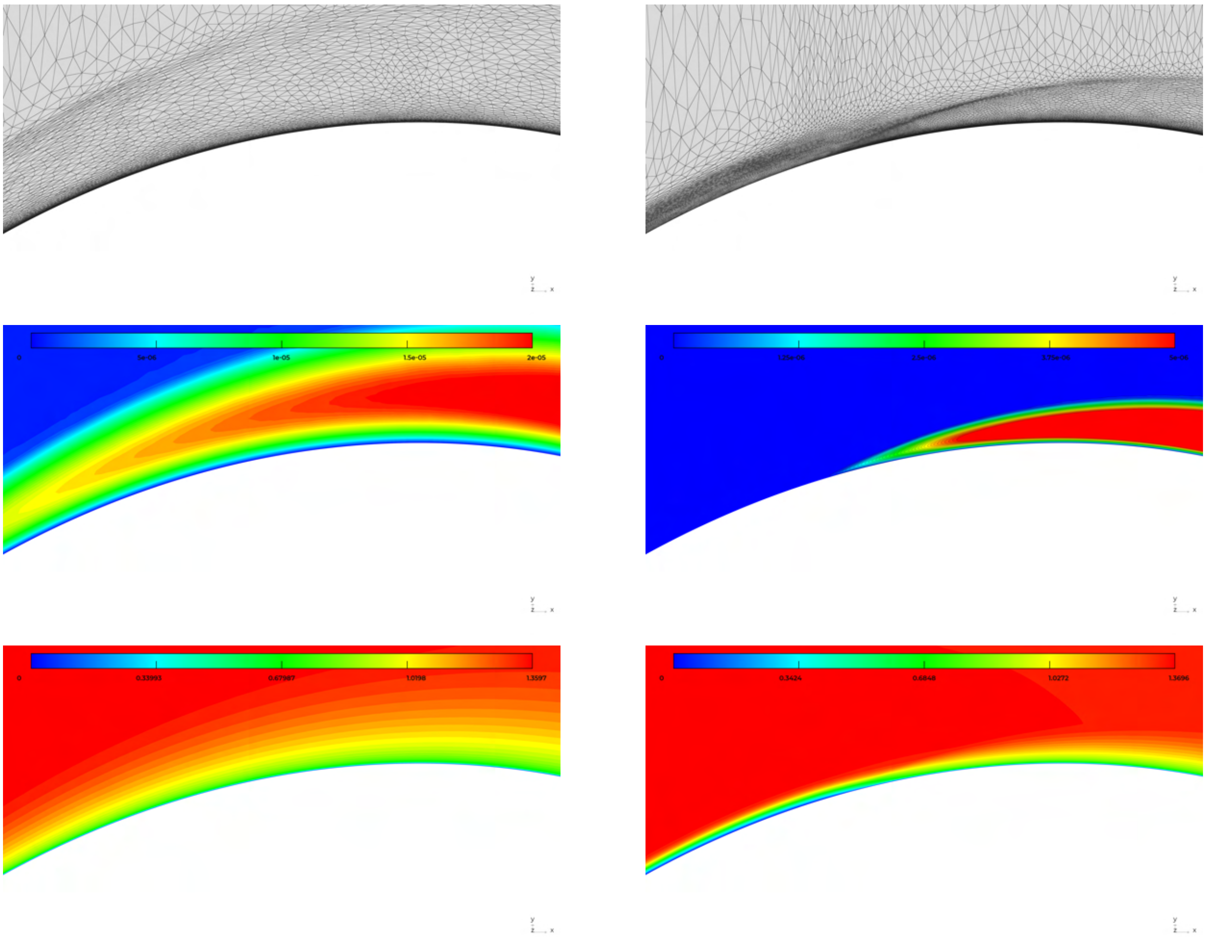

Figure 13: 2D flow past the NLF4016 airfoil at AoA = 0°. (left) GO anisotropic metric-based mesh adaptation for $30\,000$ vertices. Adapted mesh for the fully turbulent solution (left). Adapted mesh for the transitional solution (right) . Pseudo-viscosity field $\tilde{\nu}$ (middle) and streamwise velocity component field (bottom). Both meshes are stretched along the wall-normal direction by a factor 5, to the transitional region.

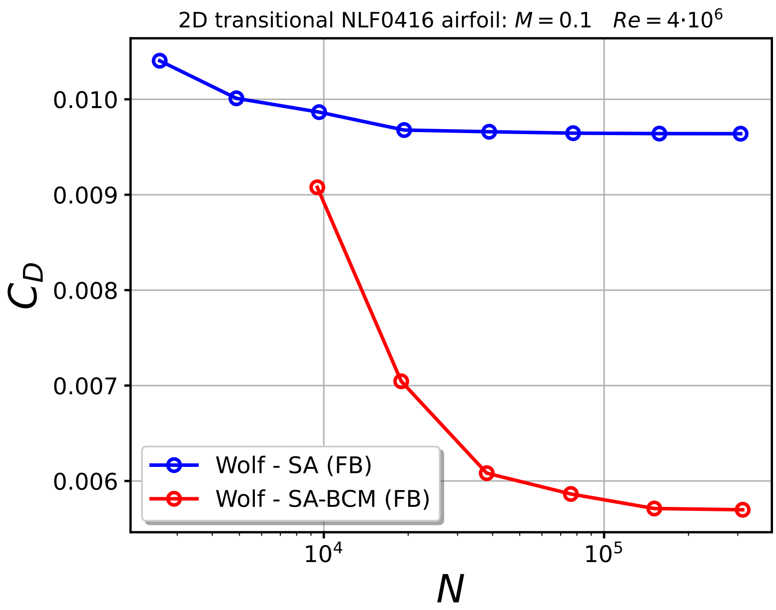

Figure 14: 2D flow past the NLF4016 airfoil at AoA = $0°$. GO anisotropic metric-based mesh adaptation. Evolution of the Drag C_D coefficient during the adaptation process. Comparison between fully turbulent calculation (blue curve) and transitional calculation (red curve).

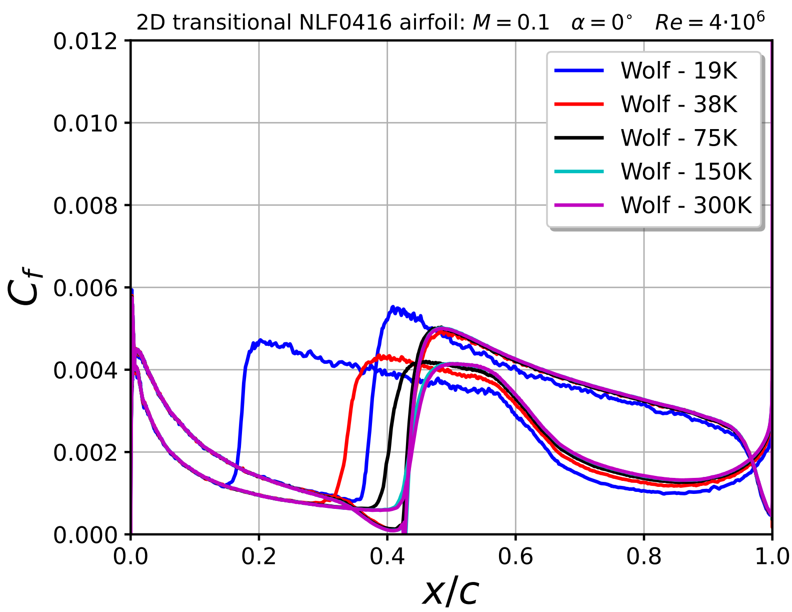

Figure 15: 2D flow past the NLF4016 airfoil at AoA = $0°$. GO anisotropic metric-based mesh adaptation. Evolution of the Skin Friction C_f coefficient during the adaptation process. The solution is mesh-converged at the $150\,000$ vertices adapted mesh.

2.5.3 Adapted calculations at different Angles of Attack

The adaptive calculations at different Angles of Attack (AoAs) are shown in Figure 16. In order to accelerate the convergence, each adaptive simulation is initialized at its corresponding adapted SA solution at $10\,000$ vertices. The process is confirmed to be robust. As expected the drag C_D and lift C_L coefficients increase with increasing AoAs. Specifically, from Figure 17 , we can observe the transition point shifting towards upstream locations. This clearly means that transition occurs earlier at higher AoAs.

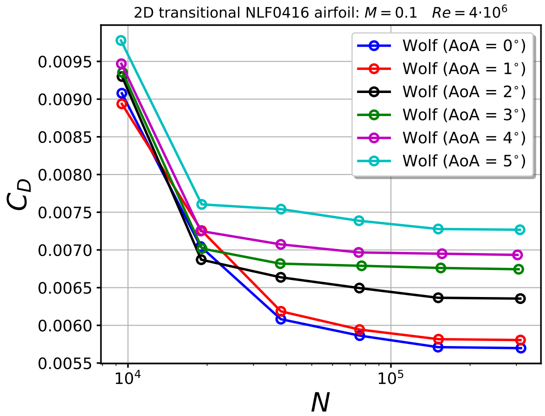

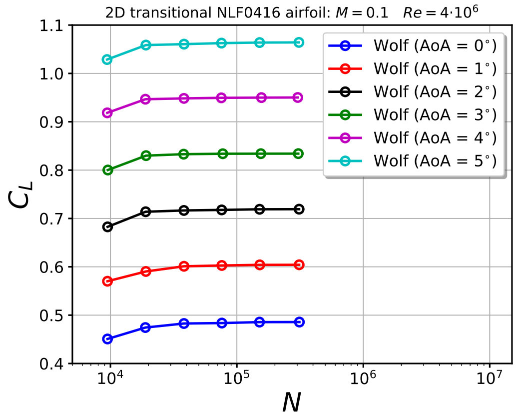

Figure 16: 2D flow past the NLF4016 airfoil at different Angles of Attack. GO anisotropic metric-based mesh adaptation. Evolution of the Drag C_D (left) and the Lift C_L coefficient, during the adaptation process. N is the number of vertices of the adapted meshes.

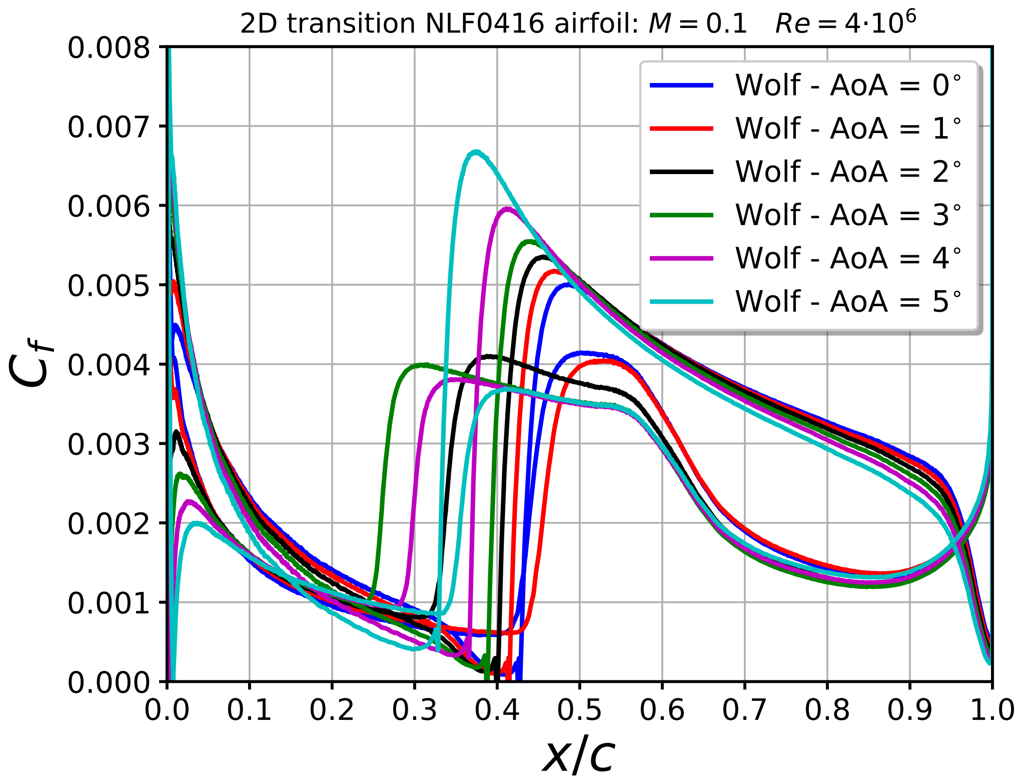

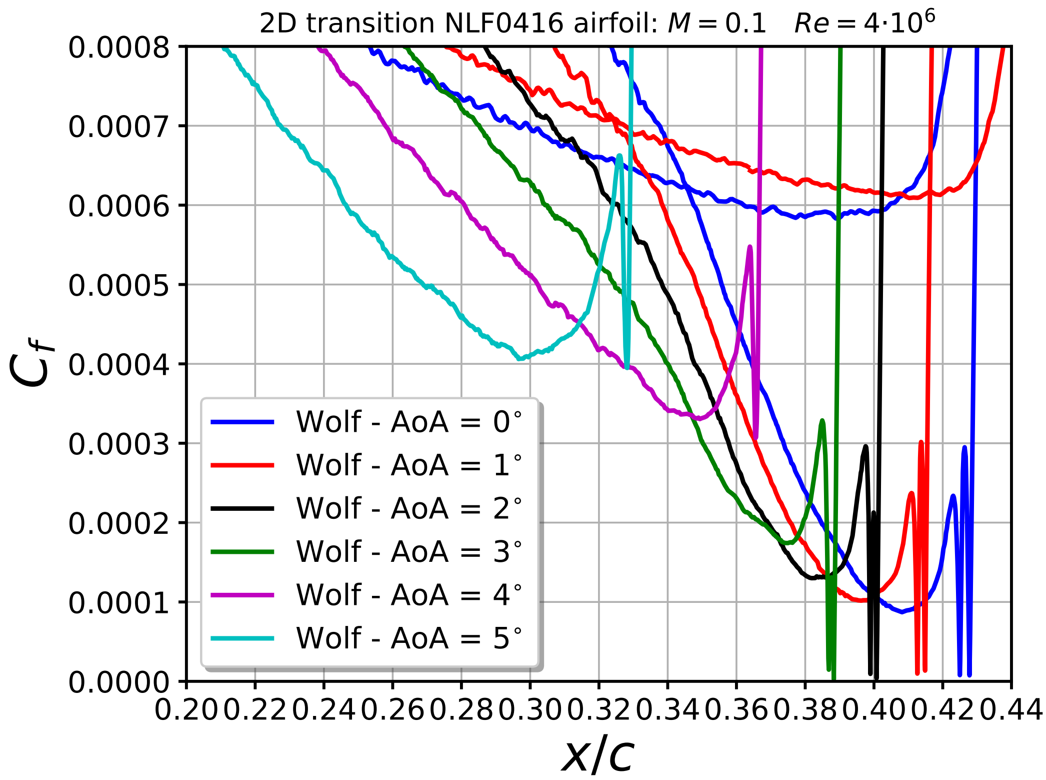

Figure 17: 2D NLF0416 GO anisotropic metric-based mesh adaptation. Evolution of the Skin Friction C_f coefficient with the Angle of Attack AoA. The adapted meshes are composed of about $300\,000$ vertices.

3 Contributions by DAV

In order to solve the RANS equations for compressible fluids, DAV uses the in-house AETHER code(10). AETHER solves the RANS equations on unstructured grids with tetrahedra. It is based on a continuous finite element method with an entropic formulation, stabilized with the Streamline Upwind Petrov-Galerkin (SUPG) method. Several one- and two-equation turbulence models are available including the Spalart--Allmaras, $k-\epsilon$, $k-\omega$, $k-kL$ models as well as Reynolds-Stress-Models. For transition modeling, the SST-2003-LM2009 and the Fehrs-2017 (15) were originally available in the code, and the SA-noft2-Gamma-Retheta was implemented in the framework of the NEXTAIR project. The implementation of the SA-sLM2015 transition model is in progress: it is actually the main target of DAV (including its adjoint-based gradient) in the framework of NEXTAIR. Tapenade differentiation in reverse mode (adjoint approach) has been successfully applied to the Fehrs-2017 model and the corresponding procedure is currently in progress for the SA-noft2-Gamma-Retheta model.

3.1 Flow around the NLF(1)--0416 Airfoil

The first case is dealing with the NLF(1)--04616 isolated airfoil; the flow conditions can be found in 1.4.2 and are not repeated herein. Comparison with experimental data, (31), and numerical results obtained by DAV (using the AETHER code) and NTUA (using the PUMA code) are presented for the $k-\omega\ SST$ and the Spalart-Allmaras turbulence models (without transition) and with the SST-2003-LM2015 and SA-noft2-Gamma-Retheta transition model in Fig. 18. In both codes, the use of transition modeling is absolutely necessary for meeting the experimental data with high accuracy. For a given model a good agreement between the two codes is observed. Cross-code comparison enables to demonstrate the correct implementation of models.

3.2 Flow and Adjoint Analysis around a Generic tail-less configuration

DAV has also studied the flow around a generic tail-less configuration, Fig. 19. The flow conditions are $M_\infty = 0.75$, AoA $= 3.5°$. The pressure and the incompressible form factor are presented in Fig. 20 where the shock wave and the transition line are captured by the Fehrs-2017, (15) transition model. The difference between the fully turbulent and laminar simulations can be seen at the pressure coefficient for a spanwise cut $y = 6000mm$ in Fig. 21.

Regarding the development of the adjoint method the sensitivity map for the pitching moment, Fig. 22, provided by the adjoint (direct approach) with and without the ``frozen transition'' assumption is compared with FDs in Fig. 23. It can be seen that the ``frozen transition'' assumption is harmful for the accuracy of the computed gradients. This is also demonstrated, in more detail, in Table 2.

Gradient	C_D	C_L	C_M
FD2	-0.00949	0.1278	-0.0147
Differentiated Transition	-0.00961	0.1312	-0.0141
Frozen Transition	-0.00929	0.1046	-0.0101
Frozen Turbulence and Transition	-0.00969	0.1025	-0.0067

Table 2: *Generic tail-less configuration*: Gradient regarding the pitching rotation angle parameter.

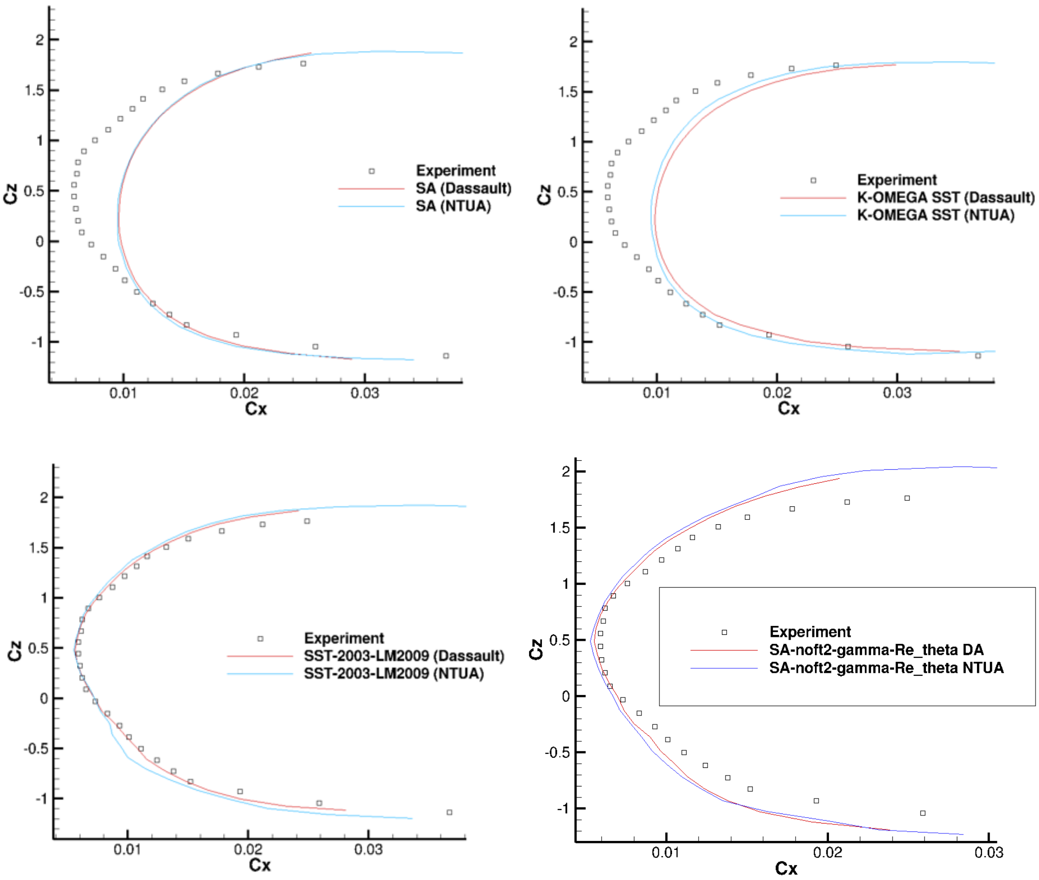

Figure 18: *NLF(1)–0416 Airfoil*: C_L (C_z) vs. C_D (C_x) polar diagrams with the $k–\omega$ SST, the Spalart-Allmaras and the SST-2003-LM2015 model. Experimental data are compared with numerical results from DAV (red curve) and NTUA (blue curve).

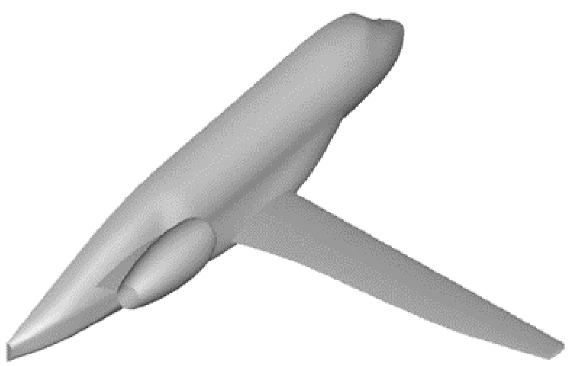

Figure 19: *Generic tail-less configuration*: Geometry

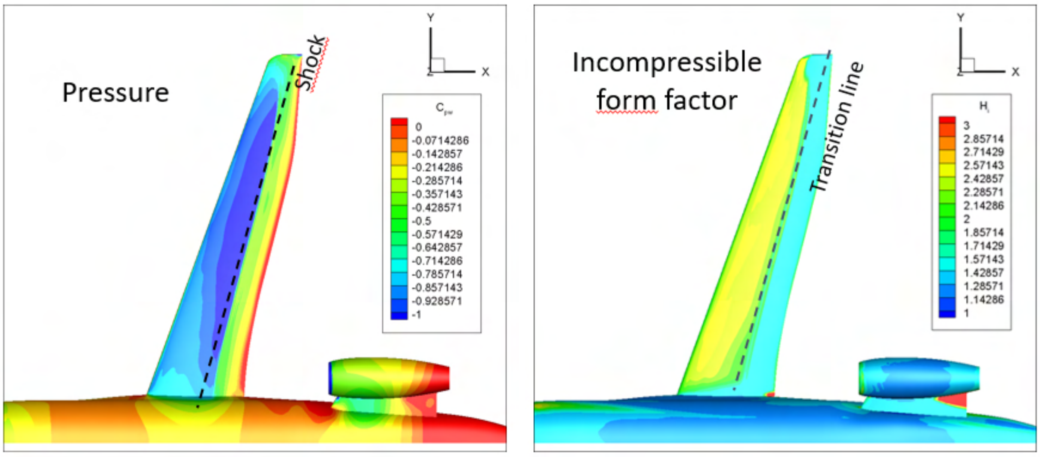

Figure 20: *Generic tail-less configuration*: Pressure field and incompressible form factor.

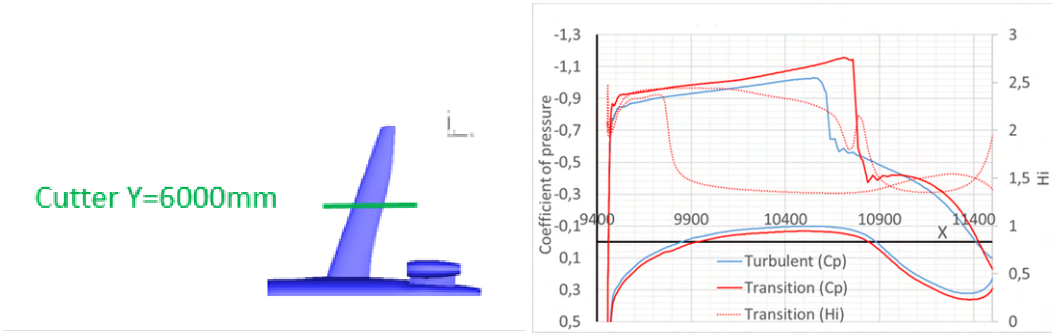

Figure 21: *Generic tail-less configuration*: Pressure distribution with fully turbulent and transitional simulation at a spanwise cut $y = 6000mm$.

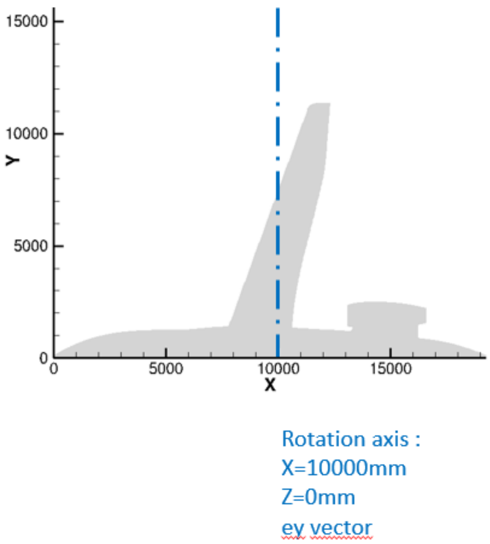

Figure 22: *Generic tail-less configuration*: Rotation axis: $x = 10000mm$, $z = 0mm$

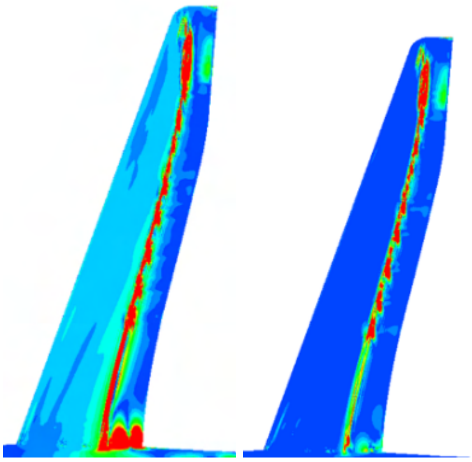

Figure 23: *Generic tail-less configuration*: Absolute difference between FDs (with second order accuracy) and linear gradient (AD Tapenade) with and without the ``frozen transition´´ assumption. Left: Linear gradient with ``frozen transition´´. Right: Linear gradient with differentiated transition.

References

(1) F. Alauzet and L. Frazza. Feature-based and goal-oriented anisotropic mesh adaptation for rans applications in aeronautics and aerospace. *Journal of Computational Physics*, 439:110340, 2021.

(2) F. Alauzet, L. Frazza, and D. Papadogiannis. Periodic adjoints and anisotropic mesh adaptation in rotating frame for high-fidelity rans turbomachinery applications. *Journal of Computational Physics*, 450:110814, 2022.

(3) F. Alauzet and A. Loseille. High-order sonic boom modeling based on adaptive methods. *Journal of Computational Physics*, 229(3):561--593, 2010.

(4) F. Alauzet and A. Loseille. A decade of progress on anisotropic mesh adaptation for computational fluid dynamics. *Computer-Aided Design*, 72:13--39, 2016.

(5) F. Alauzet and M. Mehrenberger. P1-conservative solution interpolation on unstructured triangular meshes. *International Journal for Numerical Methods in Engineering*, 84(13):1552--1588, 2010.

(6) Frédéric Alauzet. Size gradation control of anisotropic meshes. *Finite Elements in Analysis and Design*, 46(1-2):181--202, 2010.

(7) V.G. Asouti, X.S. Trompoukis, I.C. Kampolis, and K.C. Giannakoglou. Unsteady CFD computations using vertex-centered finite volumes for unstructured grids on Graphics Processing Units. *International Journal for Numerical Methods in Fluids*, 67(2):232--246, 2011.

(8) Houman Borouchaki, Frederic Hecht, and Pascal J Frey. Mesh gradation control. *International Journal for Numerical Methods in Engineering*, 43(6):1143--1165, 1998.

(9) S. C. Cakmakcioglu, O. Bas, R. Mura, and U. Kaynak. A revised one-equation transitional model for external aerodynamics. In *AIAA Aviation 2020 Forum*, page 2706, 2020.

(10) F Chalot, Z Johan, M Mallet, F Billard, L Martin, and S Barré. Extension of methods based on the stabilized finite element formulation for the solution of the navier--stokes equations and application to aerodynamic design. *Computer Methods in Applied Mechanics and Engineering*, page 116425, 2023.

(11) J. G. Coder. Standard test cases for CFD-based laminar-transition model verification and validation. In *2018 AIAA Aerospace Sciences Meeting*, 2018.

(12) J.R. Dagenhart and W. S. Saric. Crossflow stability and transition experiments in swept-wing flow. Technical Report TP-1999-209344, NASA, 1999.

(13) V. D'Alessandro, S. Montelpare, and R. Ricci. Assessment of a Spalart-Allmaras model coupled with local correlation based transition approaches for wind turbine airfoils. *Applied Sciences*, 11(4), 2021.

(14) V. D'Alessandro, S. Montelpare, R. Ricci, and A. Zoppi. Numerical modeling of the flow over wind turbine airfoils by means of Spalart-Allmaras local correlation based transition model. *Energy*, 130:402--419, 2017.

[15] M. Fehrs. One-equation transition model for airfoil and wing aerodynamics. In A. Dillmann, G. Heller, E. Krämer, C. Wagner, S. Bansmer, R. Radespiel, and R. Semaan, editors, *New Results in Numerical and Experimental Fluid Mechanics XI*, pages 199--208, Cham, 2018. Springer International Publishing.

[16] A. Jameson. Origins and further development of the jameson–schmidt–turkel scheme. *AIAA Journal*, 55:1--23, 03 2017.

[17] M.G. Kontou. *The Continuous Adjoint Method with Consistent Discretization Schemes for Transitional Flows and the Use of Deep Neural Networks in Shape Optimization in Fluid Mechanics*. PhD thesis, National Technical University of Athens, 2023 (to appear).

[18] R. Langtry. Extending the gamma-rethetat correlation based transition model for crossflow effects (invited). In *45th AIAA Fluid Dynamics Conference*, 2015.

[19] R. Langtry and F. Menter. Correlation-based transition modeling for unstructured parallelized computational fluid dynamics codes. *AIAA Journal*, 47:2894--2906, 12 2009.

[20] A. Loseille and F. Alauzet. Continuous mesh framework part I: well-posed continuous interpolation error. *SIAM J. Numer. Anal.*, 49(1):38--60, 2011.

[21] A. Loseille and F. Alauzet. Continuous mesh framework part II: validations and applications. *SIAM J. Numer. Anal.*, 49(1):61--86, 2011.

[22] A. Loseille and R. Löhner. On 3d anisotropic local remeshing for surface, volume and boundary layers. In *Proceedings of the 18th international meshing roundtable*, pages 611--630. Springer, 2009.

[23] A. Loseille and R. Lohner. Anisotropic adaptive simulations in aerodynamics. In *48th AIAA Aerospace Sciences Meeting Including the New Horizons Forum and Aerospace Exposition*, page 169, 2010.

[24] A. Loseille and R. Löhner. Boundary layer mesh generation and adaptivity. In *49th AIAA Aerospace Sciences Meeting including the New Horizons Forum and Aerospace Exposition*, page 894, 2011.

[25] V. Menier, A. Loseille, and F. Alauzet. Cfd validation and adaptivity for viscous flow simulations. In *7th AIAA Theoretical Fluid Mechanics Conference*. AIAA, 2014.

[26] F. Menter, M. Kuntz, and R. Langtry. Ten years of industrial experience with the SST turbulence model. *Turbulence, Heat and Mass Transfer*, 4, 2003.

[27] R. Mura and S. C. Cakmakcioglu. A revised one-equation transitional model for external aerodynamics-part i: Theory, validation and base cases. In *AIAA Aviation 2020 Forum*, page 2714, 2020.

[28] M. Piotrowski and D. Zingg. Smooth local correlation-based transition model for the Spalart-Allmaras turbulence model. *AIAA Journal*, 10 2020.

[29] P. Roe. Approximate Riemann solvers, parameter vectors, and difference schemes. *Journal of Computational Physics*, 43(2):357 -- 372, 1981.

[30] G. Schubauer and P. Klebanoff. Contributions on the mechanics of boundary-layer transition. Technical Report NACA-TR-1289, NASA, 1955.

[31] D. M. Somers. Design and Experimental Results for a Natural-Laminar-Flow Airfoil for General Aviation Applications. *NASA Technical Paper 1861*, 1981.

(32) D. M. Somers. Design and experimental results for a natural-laminar-flow airfoil for general aviation applications. Technical report, 1981.

(33) P. Spalart and S. Allmaras. A one-equation turbulence model for aerodynamic flows. In *30th aerospace sciences meeting and exhibit*, page 439, 1992.

(34) P. Spalart and S. Allmaras. A one-equation turbulence model for aerodynamic flows. *La Recherche Aérospatiale*, 1:5--21, 1994.

(35) J. L. Steger and R.F Warming. Flux vector splitting of the inviscid gasdynamic equations with application to finite-difference methods. *Journal of Computational Physics*, 40(2):263--293, 1981.